The Astrophysical Journal, 848:78 (16pp), 2017 October 20 https://doi.org/10.3847/1538-4357/aa8df4

Mapping the Lyα Emission around a $z \sim 6.6$ QSO with MUSE: Extended Emission and a Companion at a Close Separation

Emanuele P. Farina[1], Bram P. Venemans[1], Roberto Decarli[1], Joseph F. Hennawi[1], Fabian Walter[1,2,3], Eduardo Bañados[4,8], Chiara Mazzucchelli[1], Sebastiano Cantalupo[5], Fabrizio Arrigoni-Battaia[6], and Ian D. McGreer[7]
[1] Max Planck Institut für Astronomie, Königstuhl 17, D-69117, Heidelberg, Germany; emanuele.paolo.farina@gmail.com
[2] Astronomy Department, California Institute of Technology, MC105-24, Pasadena, CA 91101, USA
[3] National Radio Astronomy Observatory, Pete V. Domenici Array Science Center, P.O. Box O, Socorro, NM 87801, USA
[4] The Observatories of the Carnegie Institution for Science, 813 Santa Barbara Street, Pasadena, CA 91101, USA
[5] Institute for Astronomy, Department of Physics, ETH Zürich, Wolfgang-Pauli-Strasse 27, CH 8093, Zürich, Switzerland
[6] European Southern Observatory, Karl-Schwarzschild-Str. 2, D-85748, Garching bei München, Germany
[7] Steward Observatory, 933 North Cherry Avenue, Tucson, AZ 85721, USA
Received 2016 November 17; revised 2017 August 30; accepted 2017 September 13; published 2017 October 13

Abstract

We utilize the Multi Unit Spectroscopic Explorer (MUSE) on the Very Large Telescope to search for extended Lyα emission around the $z \sim 6.6$ QSO J0305−3150. After carefully subtracting the point spread function, we reach a nominal 5σ surface-brightness limit of $SB_{5\sigma} = 1.9 \times 10^{-18}$ erg s^{-1} cm^{-2} arcsec^{-2} over a 1 arcsec^2 aperture, collapsing five wavelength slices centered at the expected location of the redshifted Lyα emission (i.e., at 9256 Å). Current data suggest the presence (5σ accounting for systematics) of a Lyα nebula that extends for 9 kpc around the QSO. This emission is displaced and redshifted by 155 km s^{-1} with respect to the location of the QSO host galaxy traced by the [C II] 158 μm emission line. The total luminosity is $L(\mathrm{Ly}\alpha) = (3.0 \pm 0.4) \times 10^{42}$ erg s^{-1}. Our analysis suggests that this emission is unlikely to rise from optically thick clouds illuminated by the ionizing radiation of the QSO. It is more plausible that the Lyα emission is due to the fluorescence of the highly ionized optically thin gas. This scenario implies a high hydrogen volume density of $n_{\mathrm{H}} \sim 6$ cm^{-3}. In addition, we detect a Lyα emitter (LAE) in the immediate vicinity of the QSO, i.e., with a projected separation of ∼12.5 kpc and a line-of-sight velocity difference of 560 km s^{-1}. The luminosity of the LAE is $L(\mathrm{Ly}\alpha) = (2.1 \pm 0.2) \times 10^{42}$ erg s^{-1} and its inferred star-formation rate is SFR $\sim 1.3\,M_{\odot}$ yr^{-1}. The probability of finding such a close LAE is one order of magnitude above the expectations based on the QSO–galaxy cross-correlation function. This discovery is in agreement with a scenario where dissipative interactions favor the rapid build-up of supermassive black holes at early cosmic times.

Key words: cosmology: observations – galaxies: high-redshift – quasars: general – quasars: individual (J0305–3150)

1. Introduction

The study of QSOs at $z > 5.6$ plays a central role in our understanding of how supermassive black holes (SMBHs) and galaxies form in the early universe. Currently, there are more than 170 known QSOs at $z > 5.6$ (e.g., Fan et al. 2006; Jiang et al. 2009; Willott et al. 2010; Bañados et al. 2014, 2015a, 2016; Carnall et al. 2015; Reed et al. 2015; Venemans et al. 2015a; Jiang et al. 2016; Matsuoka et al. 2016), only 12 of which are located at $z > 6.5$ (Mortlock et al. 2011; Venemans et al. 2013, 2015b; Matsuoka et al. 2016, 2017; Mazzucchelli et al. 2017a). The host galaxies of these very first QSOs are actively forming stars, with prodigious star-formation rates SFR $> 100\,M_{\odot}$ yr^{-1} (Venemans et al. 2012, 2016), and were able to grow SMBHs with masses exceeding $M_{\mathrm{BH}} = 10^9\,M_{\odot}$ in less than 800 Myr (De Rosa et al. 2014; Venemans et al. 2015b). The assembly of such massive SMBHs at early cosmic time requires that they accrete at the Eddington (or even super-Eddington) limit throughout a large fraction of their lifetimes (e.g., Yoo & Miralda-Escudé 2004; Volonteri & Rees 2005; Volonteri 2010, 2012; Madau et al. 2014; Volonteri et al. 2015). To sustain such vigorous accretion and intense star formation, the first QSOs need the presence of copious amounts of gas in their surroundings (e.g., Di Matteo et al. 2012; Dubois et al. 2012). Possibly, this gas is aggregated in dense flows able to penetrate into the virial radius of the halo and to funnel gas onto the central SMBH (e.g., Di Matteo et al. 2012; Feng et al. 2014). If the gas in the host galaxy and in the circumgalactic medium of a QSO is illuminated by the SMBH ionizing radiation and/or the intense starburst, then it may be observable as an extended "fuzz" of fluorescent Lyα emission (Rees 1988; Haiman & Rees 2001; Alam & Miralda-Escudé 2002).

Several of these Lyα nebulae have been reported in the literature at intermediate redshifts ($z \sim 2$–4), leading to the general consensus that QSOs are frequently (50%–70%) embedded in nebulae with sizes of 10–100 kpc (e.g., Heckman et al. 1991a, 1991b; Christensen et al. 2006; Hennawi & Prochaska 2013; Roche et al. 2014; Herenz et al. 2015; Arrigoni Battaia et al. 2016). In the past years, gigantic nebulae, with projected sizes $\gtrsim$300 kpc, have also been detected (Cantalupo et al. 2014; Martin et al. 2014; Hennawi et al. 2015; Borisova et al. 2016a), suggesting the presence of large amounts of cold gas around intermediate-redshift QSOs. Complementary, the analysis of absorption features in close projected QSO pairs confirms that QSO host galaxies are surrounded (with a covering fraction ∼60% within the virial radius) by cold ($T \sim 10^4$ K), metal-enriched ($Z \gtrsim 0.1\,Z_{\odot}$) gas (Bowen et al. 2006; Hennawi et al. 2006a; Hennawi

[8] Carnegie-Princeton Fellow.

& Prochaska 2007, 2013; Decarli et al. 2009; Prochaska & Hennawi 2009; Farina et al. 2013, 2014; Prochaska et al. 2013a, 2013b, 2014; Johnson et al. 2015; Lau et al. 2016, 2017).

Despite the aforementioned achievements, the detection of these structures at $z \sim 6$ is challenging due to the rapid decrease of the surface brightness (SB) with redshift [SB $\propto (1+z)^{-4}$]. In recent years, huge efforts have been made to probe the extended Lyα emission around $z \sim 6$ QSOs with contrasting results. Decarli et al. (2012), using the Wide Field Camera 3 (WFC3) narrowband filters on the *Hubble Space Telescope* (*HST*), put strong limits on the Lyα extended emission in the proximity of the highly star-forming host galaxies of the QSOs SDSS J1148+5251 ($z = 6.42$, $L(\mathrm{Ly}\alpha) < 2.5 \times 10^{44}$ erg s^{-1}) and SDSS J1030+0524 ($z = 6.31$, $L(\mathrm{Ly}\alpha) < 3.2 \times 10^{44}$ erg s^{-1}). Conversely, the presence of a Lyα nebula has been reported in narrowband Suprime-Cam/Subaru images of the QSO CFHQS J2329−0301 at $z = 6.42$ (Goto et al. 2009) and subsequently confirmed with long-slit spectroscopy with the Echelle Spectrograph and Imager and with the DEep Imaging Multi-object Spectrograph (DEIMOS) spectrographs at the Keck II telescope (Willott et al. 2011; Goto et al. 2012). Whereas all of these observations consistently report the presence of a bright Lyα halo extending on scales of 15 kpc in the proximity of CFHQS J2329−0301, its luminosity is not well-constrained, with values that range from $L(\mathrm{Ly}\alpha) \gtrsim 1.7$–$7.5 \times 10^{43}$ erg s^{-1} (Willott et al. 2011; Goto et al. 2012) up to $L(\mathrm{Ly}\alpha) = 3.6 \times 10^{44}$ erg s^{-1} (Goto et al. 2009; see footnote 10 in Decarli et al. 2012). Recently, Roche et al. (2014) presented long-slit spectroscopic observations with the Optical System for Imaging and low Resolution Integrated Spectroscopy (OSIRIS) mounted on the Gran Telescopio Canarias of a sample of QSOs at $z > 2$, including one at $z = 5.95$ the radio-loud QSO SDSS J2228+0110. Although bright, extended Lyα emission appears ubiquitous in the Roche et al. sample at $z = 2$–3, only a tenuous detection is reported for SDSS J2228+0110, with a luminosity of $L(\mathrm{Ly}\alpha) \gtrsim 7.8 \times 10^{42}$ erg s^{-1} extending up to a scale of $\gtrsim$10 kpc. These values should be conservatively considered as lower limits. Indeed, they were computed by extracting the spectrum of the nebula over a small stripe close to the QSO emission. Additionally, a proper subtraction of the point spread function (PSF) was hindered by strong sky lines and by the low signal-to-noise ratio (S/N) of the spectrum.

The Integral-field Spectrograph Multi Unit Spectroscopic Explorer (MUSE; Bacon et al. 2010) on the Very Large Telescope (VLT) is the obvious game changer in this kind of study. It produces a spatially resolved spectrum with a spatial sampling of $0\farcs2 \times 0\farcs2$ and a nominal spectral resolution ($R = \lambda/\Delta\lambda$) ranging from $R = 1750$ at 465 nm to $R = 3750$ at 930 nm, allowing the technical limitations of previous spectroscopic and narrowband investigations, such as uncertainties in the systemic redshift of the QSOs, filter and slit losses, and difficulties in performing a proper PSF subtraction, to be overcome.

In this paper, we present a deep MUSE integration aimed at detecting the Lyα nebular emission around the high-redshift QSO J0305−3150 ($z = 6.61$; with an absolute magnitude at 1450 Å of $M_{1450} = -25.96 \pm 0.06$) discovered by Venemans et al. (2013) using the VISTA Kilo-Degree Infrared Galaxy (VIKING) survey. Sensitive near-infrared spectroscopy observations obtained with the Folded-port InfraRed Echellette spectrograph (FIRE) mounted on the Magellan Telescope revealed the presence of an SMBH with $M_{\mathrm{BH}} = (0.95$–$1.20) \times 10^9\,M_\odot$ accreting with an Eddington ratio $\lambda_{\mathrm{Edd}} = L_{\mathrm{Bol}}/L_{\mathrm{Edd}} = 0.68$–$0.74$ (De Rosa et al. 2014). The [C II] 158 μm emission line ($L_{[\mathrm{CII}]} = (3.9 \pm 0.2) \times 10^9\,L_\odot$, FWHM $= 255 \pm 12$ km s^{-1}) and the underlying far-infrared continuum were detected by Venemans et al. (2016) using the Atacama Large Millimeter/submillimeter Array (ALMA). From these measurements, the precise systemic redshift and SFR of the QSO host galaxy can be inferred. Although QSO redshifts derived from broad emission lines are subject to systematic shifts and large uncertainties (e.g., Richards et al. 2002; Bonning et al. 2007; Hewett & Wild 2010), especially at $z > 6$ (Venemans et al. 2016; Mazzucchelli et al. 2017a), the narrow [C II] line accurately traces the systemic redshift ($z_{\mathrm{sys}} = 6.6145 \pm 0.0001$). In addition, by fitting the FIR continuum spectrum with a modified blackbody with a spectral index $\beta = 1.6$ (after correcting for the impact of the cosmic microwave background; da Cunha et al. 2013), Venemans et al. (2016) obtained a dust temperature of 30 K and a total far-infrared luminosity of $L_{\mathrm{TIR}} = 2.6 \times 10^{12}\,L_\odot$. The investigation of the spectral energy distribution (SED) of high-z QSOs suggests that the dust emission is predominantly powered by star formation especially at $\lambda \gtrsim 100$ μm rest frame (e.g., Leipski et al. 2014; Barnett et al. 2015; see also Valiante et al. 2011). This implies[9] $\mathrm{SFR}_{\mathrm{TIR}} = 545\,M_\odot$ yr^{-1}. Aside from PSO J036+03 (Bañados et al. 2015b; Venemans et al. 2015b), J0305−3150 shows the highest SFR and Eddington ratio among the $z > 6.5$ QSOs known to date. It is thus an excellent target to constrain the properties of the gas reservoir that is expected to surround the first QSOs, together with its close environment.

Throughout this paper, we assume a concordance cosmology with $H_0 = 70$ km s^{-1} Mpc^{-1}, $\Omega_{\mathrm{M}} = 0.3$, and $\Omega_\Lambda = 1 - \Omega_{\mathrm{M}} = 0.7$. In this cosmology, at $z = 6.6145$, the universe is 0.808 Gyr old, and an angular scale $\theta = 1''$ corresponds a proper transverse separation of 5.4 kpc.

2. Observations and Data Reduction

J0305−3150 was observed with MUSE on 2014 December 15 and 2015 January 15.[10] The total time on source of 2.4 hr was divided into three observing blocks (OBs) of 48 m each, pointing to three different locations within $4''$ from the QSO. For each OB, three 960 s exposures were taken, dithering using random offsets within a $7\farcs5$ box. The Differential Image Motion Monitor (DIMM) seeing during the observations was mostly sub-arcsecond, ranging from $0\farcs7$ to $1\farcs1$ (with a median of $0\farcs8$).

We employed the MUSE Data Reduction Software (version 1.0.1; Weilbacher et al. 2012, 2014) to perform, on each of the individual exposures, bias subtraction and flat-field, twilight, and illumination corrections, as well as wavelength and flux calibrations (the latter using the standard stars HD 49798 and GD 71 observed at the beginning of each observing night).

[9] Assuming a fixed dust temperature of $T_d = 47$ K (a value commonly observed in high-redshift QSO studies; e.g., Beelen et al. 2006), the estimated FIR luminosity of J0305−3150 would be a factor of ∼2 higher ($L_{\mathrm{FIR}} = (4.0$–$7.5) \times 10^{12}\,L_\odot$) and the SFR would be in the range 940–1580 $M_\odot$ yr^{-1}. However, current data suggest a lower dust temperature for J0305−3150 (Venemans et al. 2016). In the remainder of the paper, we will thus consider 545 $M_\odot$ yr^{-1} as the bona fide SFR for the QSO's host galaxy.

[10] Programme ID: 094.B-0893(A), PI: B. P. Venemans.

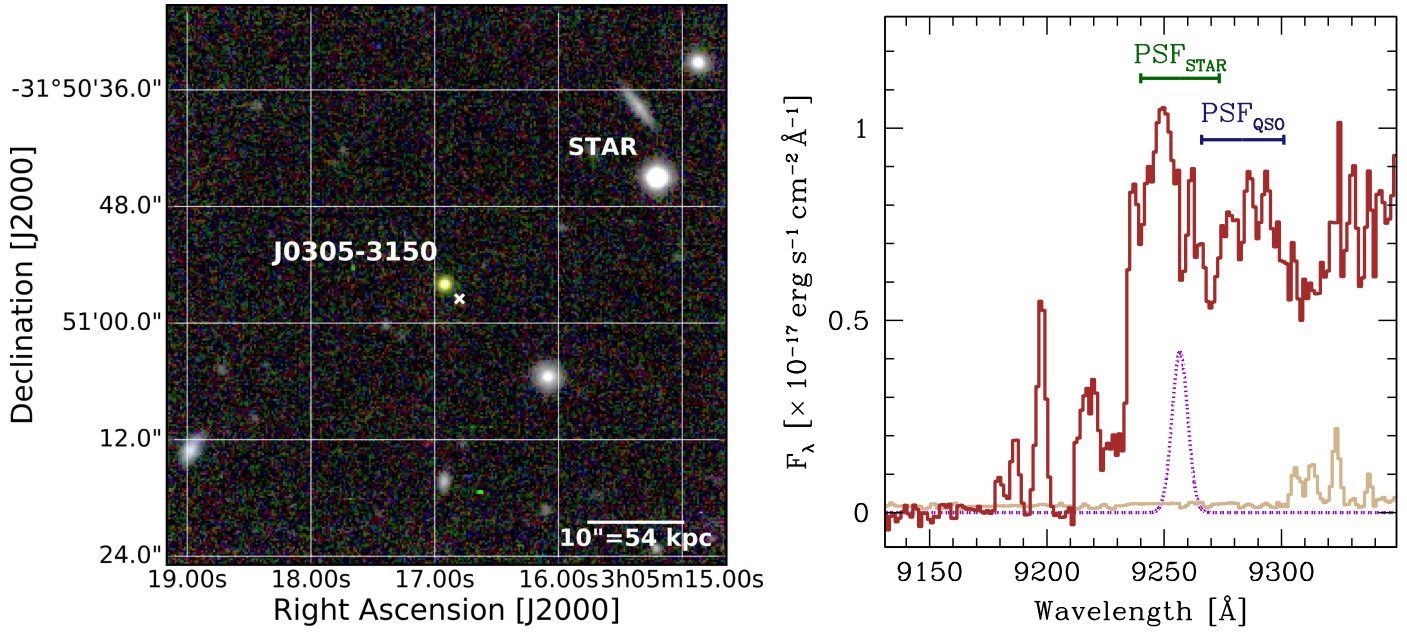

Figure 1. Left panel: false color RGB image of the field of J0305−3150 generated from the MUSE datacube (the wavelength regions used to create the figure are red = 9262 Å–9292 Å, green = 9231 Å–9261 Å, and blue = 9200 Å–9230 Å). The QSO and the star used for the PSF subtraction are labeled (see Section 3.1). The white cross marks the position of the possible Lyα emitter identified $\sim 2''$ from the QSO (see Section 4). Right panel: zoom-in of the spectrum of J0305−3150 extracted over an aperture with $0''.74$ radius from the MUSE datacube (dark brown solid line); 1σ flux uncertainties are shown in light brown. The purple dotted line shows a Gaussian emission line at the expected Lyα location with an FWHM of 255 km s^{-1}, as the [C II] line (Venemans et al. 2016; flux normalization is arbitrary), though scattering effects, could affect this shape. The solid blue bar highlights the wavelength range used to construct the empirical $\mathrm{PSF_{QSO}}$ model (from 9266 Å to 9301 Å), and the solid green one marks the region used to built $\mathrm{PSF_{STAR}}$ (from 9240 Å to 9273 Å; see Section 3.1).

Flat-field correction and sky subtraction of each exposure were improved using the CubExtractor package (S. Cantalupo 2017, in preparation). Exposures of each OB were sampled to a common grid ($0''.2 \times 0''.2 \times 1.25$ Å) and then average-combined. The absolute flux calibration for the resulting datacubes was obtained by rescaling the flux of the bright sources present in the MUSE field of view to our *i*-band images collected with the ESO Faint Object Spectrograph and Camera 2 (EFOSC2) on the New Technology Telescope (NTT; see Venemans et al. 2013 for details). Uncertainties on the absolute flux calibration resulting from this procedure are on the order of 5%. As a final step, the three datacubes were average-combined. The astrometry solution was refined by matching sources in the datacube with the first data release of the VIKING catalog (Edge et al. 2013).

The MUSE pipeline also provides a datacube containing errors formally propagated throughout the reduction process. As observed by Bacon et al. (2015), however, this process does not take into account correlations between neighboring voxels, ending up underestimating the real noise properties of the datacube. To have more realistic uncertainties, for each wavelength slice, the average of the variance delivered by the pipeline was rescaled to match the variance of the background (i.e., after removing the contribution from bright sources; see Borisova et al. 2016a for a similar approach).

In the final datacube, at 9256 Å (i.e., at the wavelength slice where the Lyα emission of the QSO is redshifted to), the FWHM of the PSF is $0''.58$, corresponding to 3.1 kpc at the QSO's redshift. The 5σ SB limit estimated after collapsing five wavelength slices centered at 9256 Å (i.e., from 9253.5 Å to 9258.5 Å) is $\mathrm{SB}^{\mathrm{l}}_{5\sigma,\lambda} = 1.9 \times 10^{-18}$erg s^{-1} cm^{-2} arcsec^{-2} over a 1 arcsec^2 aperture (see Section 3.2). The MUSE false color RGB image and the spectrum of J0305−3150 extracted over a radius of 3.7 spaxel ($0''.74$) are shown in Figure 1. Flux errors on the spectrum ($\sigma_{A,\lambda}$) are calculated from the final datacube as

$$\sigma_{A,\lambda} = \sqrt{\sum_{i \in A} \sigma^2_{\lambda,i}}, \quad (1)$$

where A is the area over which the spectrum is extracted in each wavelength slice (λ) and $\sigma^2_{\lambda,i}$ is the variance in the corresponding spaxels.

3. Recovering Extended Emission

In the following sections, we describe the procedure adopted to investigate the presence of an extended Lyα emission (Section 3.1) and to estimate the sensitivity reached in the reduced datacube (Section 3.2). Finally, in Section 3.3, we present the results of this analysis.

3.1. PSF Subtraction

An accurate PSF subtraction is necessary to recover the faint signal of the diffuse Lyα halo emerging from the PSF wings of the bright unresolved nuclear component. To perform this task, we created two empirical PSF models: $\mathrm{PSF_{QSO}}$, constructed directly from the QSO emission by collapsing regions of the spectrum virtually free from any extended emission[11] (i.e., away from the Lyα emission; see Figure 1), and $\mathrm{PSF_{STAR}}$, obtained from the bright star located $\sim 25''$ northwest from the QSO by summing up its emission over the wavelength range where the extended Lyα emission is expected to fall (see

[11] In principle, the UV continuum light from the QSO host galaxy may contribute to the wings of $\mathrm{PSF_{QSO}}$. However, in $z > 5.5$ QSOs, this emission is expected to be feeble (e.g., Mechtley et al. 2012). Given the relatively small wavelength range used to built the PSF model, we consider this contribution negligible.

Figure 1). These two PSF models are subject to different systematics, allowing us to check for the reliability of a possible detection of extended emission. The first model allows us to directly subtract the PSF contribution from the QSO without any spatial shift. However, PSF_{QSO} has a relatively low S/N due to the faintness of the source and the small range in wavelength used (starting 325 km s^{-1} away from the QSO systemic redshift, i.e., at 9266 Å, up to the wavelength where the presence of strong sky emission lines drastically increase the variance, i.e., 9301 Å; see Figure 1). In addition, it may be contaminated by the wings of the possible extended emission if they are particularly broad and/or redshifted. PSF_{STAR} instead benefits from a higher S/N, and it minimizes PSF changes with wavelength. On the other hand, it is subject to resampling to centroid the PSF model on the QSO, and to the the spatial variation of the PSF.

To subtract the unresolved QSO emission and to recover the Lyα nebula, we adapted the technique used by Hennawi & Prochaska (2013) and Arrigoni Battaia et al. (2015a) to the three-dimensional structure of the MUSE data. First, at each wavelength slice, the PSF model is rescaled to the QSO's flux estimated in a circle with radius 2 spaxel (0.″4). The underlying assumption is that the QSO is dominating the emission in this central region. A bright, centralized nebular component may, however, lead to an overestimate of the QSO's emission and thus to an underestimate of the total flux of the possible extended emission. Then, we defined the $\chi_{\lambda,i}$ datacube,

$$\chi_{\lambda,i} = \frac{\mathrm{DATA}_{\lambda,i} - \mathrm{MODEL}_{\lambda,i}}{\sigma_{\lambda,i}}, \quad (2)$$

where the indices λ and i indicate the wavelength slice and the 2D spaxel position, respectively; $\mathrm{DATA}_{\lambda,i}$ is the datacube; $\mathrm{MODEL}_{\lambda,i}$ is the rescaled PSF model; and $\sigma_{\lambda,i}$ is the square root of the variance datacube. If our model accurately describes the PSF (and in the absence of systematics), at each wavelength slice the distribution of $\chi_{\lambda,i}$ values should follow a Gaussian centered on zero with unit variance. Under this condition, this datacube thus permits the statistical significance of any putative detection to be assessed. Note that both PSF_{QSO} and PSF_{STAR} have, by construction, a much higher S/N than the QSO in a single wavelength slice; therefore, the contribution of the PSF model to the variance budget is negligible. We also constructed a smoothed datacube, $\mathrm{SMOOTH}[\chi_{\lambda,i}]$, that is helpful for identifying the possible presence of extended emission,

$$\mathrm{SMOOTH}[\chi_{\lambda,i}] = \frac{\mathrm{CONVOL}[\mathrm{DATA}_{\lambda,i} - \mathrm{MODEL}_{\lambda,i}]}{\sqrt{\mathrm{CONVOL}^2[\sigma^2_{\lambda,i}]}}, \quad (3)$$

where CONVOL indicates a convolution in the spatial axis with a 2D Gaussian kernel with $\sigma = 1$ spaxel, while $\mathrm{CONVOL}^2[\sigma^2_{\lambda,i}]$ is the convolution of the variance datacube ($\sigma^2_{\lambda,i}$) with the square of the same kernel. In the absence of systematics, spaxel values in this smoothed images should still follow a Gaussian distribution, but with smaller variance due to the increased correlation among pixels. The extended Lyα nebulae around radio-quiet QSOs typically show quiescent kinematics with FWHM $\lesssim$ 600 km s^{-1} (Arrigoni Battaia et al. 2015b; Borisova et al. 2016a). We therefore repeat the same procedure, binning over 3, 5, 10, and 15 wavelength slices in order to maximize the S/N of the emission with FWHMs of ∼120, 200, 400, and 600 km s^{-1}. The resulting $\chi_{\lambda,i}$ and $\mathrm{SMOOTH}[\chi_{\lambda,i}]$ datacubes were then visually inspected to search for the presence of any extended emission.

3.2. Detection Limits

The detection limit for a Lyα nebular emission in the MUSE datacube depends on its FWHM and physical size: lower SB levels can be reached by averaging in space and/or in velocity. Under the (erroneous) assumption that spaxels are independent, the theoretical detection limits for an extended source in a single wavelength slice is given by $\mathrm{SB}^A_{1\sigma,\lambda} = \mathrm{SB}_{1\sigma,\lambda}/\sqrt{\#_A}$, where $\mathrm{SB}_{1\sigma,\lambda}$ is the 1σ SB detection limit per $0.''2 \times 0.''2$ spaxel at the wavelength slice λ and $\#_A$ is the number of spaxels in the isophotal area of the source A. The corresponding limit on the total flux (and thus on the luminosity) can be written as $F^A_{1\sigma,\lambda} = \mathrm{SB}_{1\sigma,\lambda}\sqrt{\#_A}\,\mathrm{PS}^2$, where PS is the pixel scale of MUSE: PS = 0.″2 spaxel^{-1}. Binning the MUSE datacube over 3, 5, 10, and 15 wavelength slices centered at 9256 Å (i.e., at the expected position of the Lyα emission), the formal 5σ SB detection limits calculated over an aperture of 1 arcsec^2 are $\mathrm{SB}^1_{5\sigma,\lambda} = [1.3,\ 1.9,\ 3.4,\ 5.0] \times 10^{-18}$ erg s^{-1} cm^{-2} arcsec^{-2}, respectively.

The noise properties of the MUSE datacube are, however, not uniform. In addition, cross-talk between voxels and systematics introduced during data reduction and PSF subtraction will alter these theoretical detection limits. We tested the reliability of the calculated SB limits by introducing a set of synthetic sources in the PSF-subtracted datacubes and visually estimated the level of a convincing detection. For this purpose, we focused on the wavelength region where a Lyα line redshifted to z_{sys} would fall (i.e., at 9256 Å), and we binned the datacube over the same wavelength slices used for the sources detection (see Section 3.1). We randomly placed mock circular sources (including Poisson noise) with a top-hat SB in different locations in each pseudo-narrowband images. These mock sources have total integrated luminosities $L_{\mathrm{mock}} = 10^{[41.5,\ 42.2,\ 42.9,\ 43.6,\ 44.3]}$ erg s^{-1}, diameters $d_{\mathrm{mock}} = [3,\ 5,\ 25,\ 50,\ 100]$ kpc, and, in the wavelength space, a Gaussian distribution with $\mathrm{FWHM}_{\mathrm{mock}} = [80,\ 120,\ 200,\ 400,\ 600]$ km s^{-1} (where 80 km s^{-1} is, roughly, the nominal resolution limit and the other values match the binning considered in the PSF subtraction process; see Section 3.1). A diameter of $d_{\mathrm{mock}} = 3$ kpc corresponds to the seeing measured in the datacube and is hence unresolved.

As an illustrative example, we show in Figure 2 how synthetic sources with $\mathrm{FWHM}_{\mathrm{mock}} = 120$ km s^{-1} and different d_{mock} and L_{mock} would appear in a pseudo-narrowband image obtained by collapsing three wavelength slices around the expected position of the Lyα line (i.e., from 9254.75 Å to 9257.25 Å). The corresponding χ_i and $\mathrm{SMOOTH}[\chi_i]$ images (Figure 3) show that we should be able to visually detect these sources down to $L(\mathrm{Ly}\alpha) \sim 10^{42.0}$ erg s^{-1} if unresolved and down to $L(\mathrm{Ly}\alpha) \sim 10^{44.0}$ erg s^{-1} if the emission is more extended.

If sources fall on the top of the QSO emission, the PSF subtraction process will hinder the achievement of the theoretical detection limits. However, the QSO is relatively faint in the datacube, and PSF wings quickly drop below the 2σ SB limit. For instance, in the pseudo-narrowband obtained by collapsing the datacube between 9238.5 Å and 9242.0 Å, the

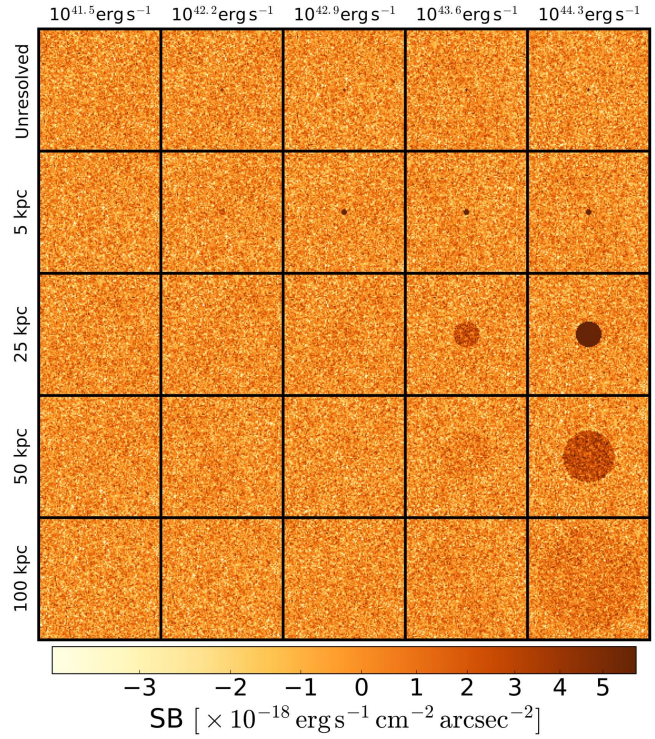

Figure 2. Illustration of how synthetic sources, created using the procedure described in Section 3.2, would appear in a pseudo-narrowband image obtained by binning the [$\mathrm{DATA}_{\lambda,i}$ − $\mathrm{MODEL}_{\lambda,i}$] datacube over three wavelength slices (i.e., ∼120 km s^{-1}) around the expected position of the Lyα emission. The nominal 5σ SB limit reached in this pseudo-narrowband image is $\mathrm{SB}^{1}_{5\sigma,\lambda}$ = 1.3 × 10^{-18} erg s^{-1} cm^{-2} arcsec^{-2} over a 1 arcsec^2 aperture. At the center of each box is plotted a source with fixed $\mathrm{FWHM}_{\mathrm{mock}}$ = 120 km s^{-1}, total luminosity ranging from $L_{\mathrm{mock}} = 10^{41.5}$ erg s^{-1} to $10^{44.3}$ erg s^{-1} (increasing from the left to the right of the x-axis), and diameter going from d_{mock} = 3 kpc (i.e., unresolved) to 100 kpc (increasing from top to the bottom of the y-axis). Note that assuming a Gaussian shape for the line emission, only roughly half of the total flux falls in the pseudo-narrowband image shown here. Each box has a size of 22″ × 22″.

QSO radial profile becomes consistent with zero (at 2σ) at a separation of ∼1.″2 (i.e., ∼6.5 kpc at z_{sys}; see Figure 4). Contamination due to imperfect PSF subtraction are therefore expected to impact only sub-arcsecond separations.

3.3. Tentative Detection of an Extended Emission

Figure 5 shows the result of the PSF subtraction procedure described above. A Lyα extended emission with a size of ∼1.″6 (∼9 kpc) toward the southwest of J0305−3150 is tentatively detected in the DATA_i − MODEL_i pseudo-narrowband image obtained by collapsing the three wavelength slices from 9259.75 Å to 9262.25 Å. After removing a circle of 0.″4 radius centered on the QSO's position (to avoid possible contamination due to imperfect PSF subtraction,) we measured the flux integrated over an elliptical aperture, with semiminor and semimajor axes of 0.″9 and 1.″4. We obtained $F(\mathrm{Ly}\alpha)$ = (6.1 ± 0.8) × 10^{-18} erg s^{-1} cm^{-2} ($F(\mathrm{Ly}\alpha)$ = (5.6 ± 0.8) × 10^{-18} erg s^{-1} cm^{-2}) using $\mathrm{PSF}_{\mathrm{QSO}}$ ($\mathrm{PSF}_{\mathrm{STAR}}$) as our model, yielding a 7.6σ (7.0σ) detection. The inferred luminosity of the extended emission is $L(\mathrm{Ly}\alpha) = (3.0 \pm 0.4) \times 10^{42}$ erg s^{-1} (using $\mathrm{PSF}_{\mathrm{QSO}}$), more than one order of magnitude fainter with respect to the characteristic luminosity of LAEs at $z \sim 6.6$ (e.g., Hu et al. 2010; Matthee et al. 2015).

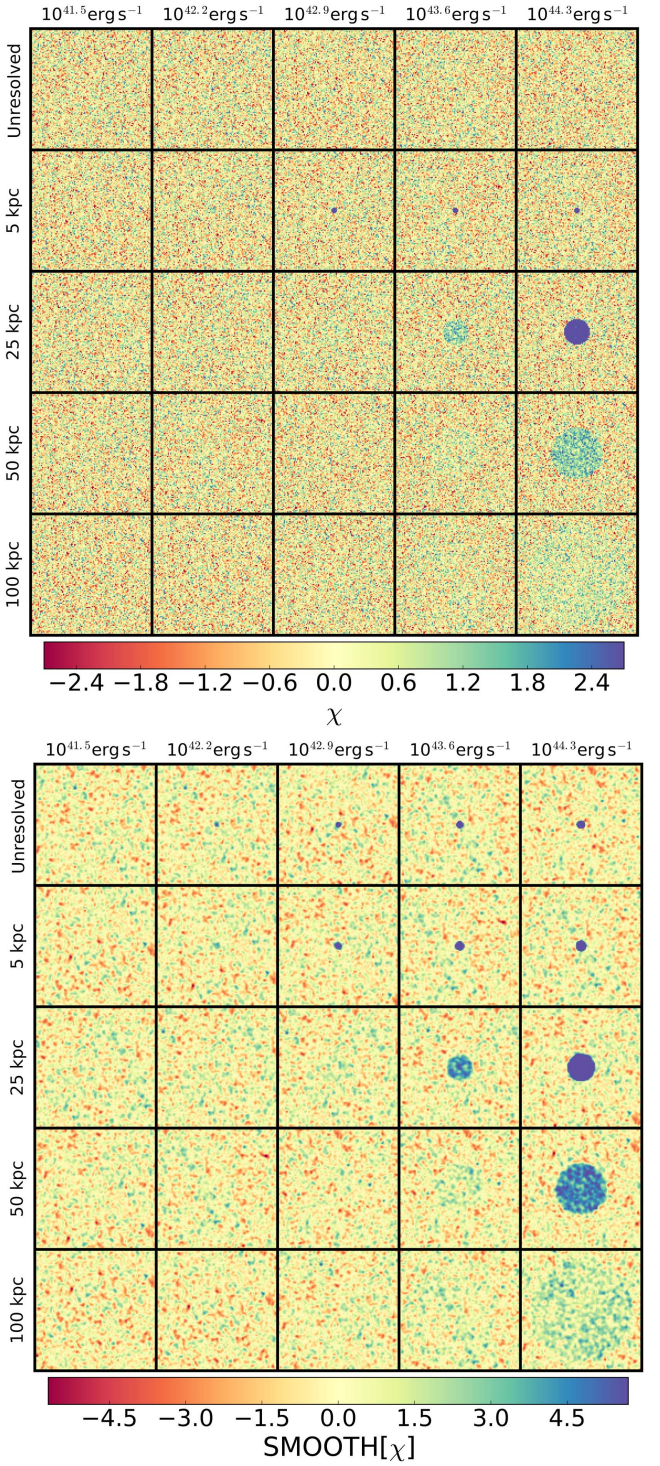

Figure 3. χ_i (top panel; see Equation (2)) and SMOOTH[χ_i] (bottom panel; see Equation (3)) pseudo-narrowband images of the synthetic sources shown in Figure 2. In the absence of systematics, χ_i displays the statistical significance of the emission in each spaxel. The smooth process introduces correlation among neighbor spaxels. This enhances the coherent signal coming from close positive spaxels, allowing us to increase our ability to detect faint extended sources (note the different scales of the color bars). At a fixed luminosity, this process is more sensitive to compact objects rather than diffuse emissions. The nominal 5σ detection limits are $L_{5\sigma} = 10^{[41.9,42.1,42.8,43.1,43.4]}$ erg s^{-1} for sources with d_{mock} = [3, 5, 25, 50, 100] kpc, respectively. The size of each box is the same as in Figure 2.

In order to assess the reliability of this detection, we empirically estimate the effects of systematics in the pseudo-narrowband image obtained by collapsing the $\mathrm{DATA}_{\lambda,i}$ − $\mathrm{MODEL}_{\lambda,i}$

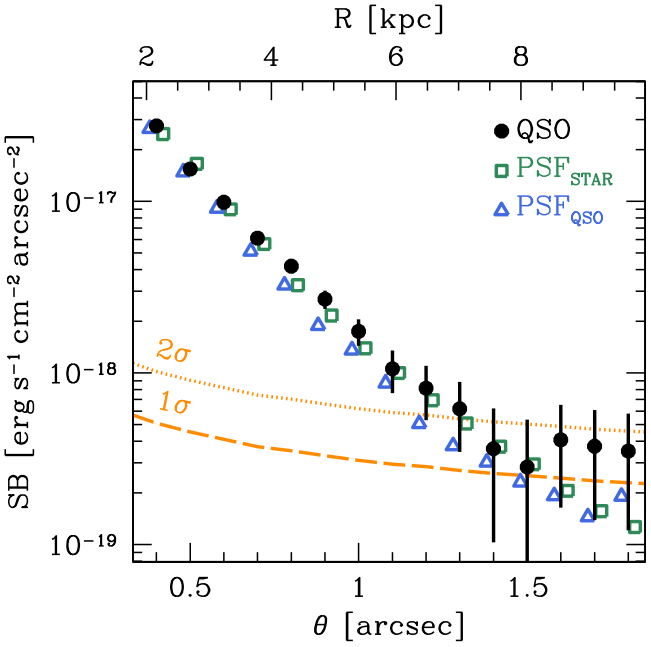

Figure 4. Radial profile of the QSO emission extracted within annuli evenly spaced by 0.″2 in the pseudo-narrowband image created by collapsing the datacube over three wavelength slices between 9238.5 Å and 9242.0 Å (i.e., where the QSO emission peaks and contamination from the possible extended emission is expected to be absent; black dots). For comparison, the rescaled PSF_{STAR} (green squares) and PSF_{QSO} (blue triangles) are also shown (points are artificially shifted on the x-axis to avoid superposition). The two PSF models appear in good agreement with the QSO profile. The region at angular separation $\theta < 0.''4$ is used to normalize the PSF models (see Section 3.1) and therefore is not plotted here. The nominal 5σ SB limit reached in this image is $SB^{1}_{5\sigma,\lambda} = 1.2 \times 10^{-18}$ erg s^{-1} cm^{-2} arcsec^{-2} over a 1 arcsec^2 aperture. The orange dashed and dotted lines mark the corresponding 1σ and 2σ limits, respectively. The wings of the QSO emission become consistent with the noise at separations larger than $\gtrsim 1.''5$ (at 1σ). Our ability to detect extended emission at these scales is thus not influenced by the PSF subtraction procedure.

datacube over the wavelength range 9259.75 Å to 9262.25 Å (see Arrigoni Battaia et al. 2015a for a similar test performed on narrowband images). From this image, we extracted the fluxes and variances for a set of elliptical apertures, randomly picking background locations (i.e., avoiding bright sources) in an annulus with internal and external radii of 5″ and 25″ from the QSO, respectively. In the absence of systematics, the flux over noise ratio of these apertures should follow a Gaussian distribution centered on zero and with $\sigma = 1$. Figure 6 shows that the actual distribution is nearly Gaussian with an offset of −0.28 and a sigma 1.42× broader. These deviations could be due to poor sky subtraction and/or to 3D correlations present in the MUSE datacube. Taking into account systematics, the significance of our detection is reduced to 5.3σ (4.9σ) using PSF_{QSO} (PSF_{STAR}) as the PSF model.

The spectrum of this possible nebula extracted from the $DATA_{\lambda,i} - MODEL_{\lambda,i}$ datacube over the same elliptical aperture considered above is shown in Figure 7. The possible Lyα halo appears as the strongest feature present within ± 1000 km s^{-1} from the QSO's systemic redshift. This narrow emission-line peaks at $\lambda = 9261.5$ Å and has an FWHM = 65 km s^{-1}. The fitted width is slightly smaller than the nominal resolution limit of MUSE at these wavelengths, but consistent given the low S/N per spectral bin of the line. Under the assumption that we are probing the Lyα emission, the line appears redshifted by 155 km s^{-1} with respect to the systemic redshift traced by the [C II] line. This is smaller than the 445 km s^{-1} shift observed between the Hα emission (originating from H II regions in the galaxy) and the Lyα line in low-redshift UV-selected galaxies (e.g., Steidel et al. 2010), but in agreement with the 175 km s^{-1} offset seen in strong Lyα emitters (LAE) at $z \sim 2$ (e.g., Hashimoto et al. 2013). A similar shift is also observed at higher redshift. For instance, Pentericci et al. (2016) observed shifts of 100–200 km s^{-1} between the Lyα and [C II] emission line in four galaxies at redshifts between 6.6 and 7.2. Likewise, the Lyα emission of the $z \sim 6$ star-forming galaxy A383-5.2 appears to be shifted by 120 km s^{-1} with respect to the systemic redshift probed via the C III] λ1909 metal line (Stark et al. 2015).

4. Searching for Lyα Emitters

The rapid formation of SMBHs in the early universe may imply that the first QSOs are tracers of galaxy overdensities. In fact, the black hole growth may be fostered by rich environments, where interactions and mergers are more likely to occur (see Volonteri 2012 for a review). To test this hypothesis, we performed a search of LAEs in the proximity of J0305−3150.

To identify LAEs associated with the QSO, we focused our attention on the wavelength range between ∼9226 Å and ∼9287 Å, corresponding to ±1000 km s^{-1} from the QSO systemic redshift. This region was recursively sliced in 10 Å wide (i.e., ∼325 km s^{-1}) pseudo-narrowband images. The nominal 5σ SB limit reached in the image centered at 9256 Å is $SB^{1}_{5\sigma,\lambda} = 2.3 \times 10^{-18}$ erg s^{-1} cm^{-2} arcsec^{-2} over a 1 arcsec^2 aperture. Assuming a spatially unresolved line emission with FWHM of 270 km s^{-1} (i.e., the FWHM of the $z \sim 6.6$ LAE spectral template presented in Ouchi et al. 2010), the corresponding 5σ luminosity limit is $L_{5\sigma} = 6.7 \times 10^{41}$ erg s^{-1}. Each image was then processed using SExtractor (Bertin & Arnouts 1996) requiring a minimum detection area of 7 spaxel and a detection threshold of 1.5σ. Identified sources were considered only if located within a 50″ × 50″ box centered on the QSO. This search box, smaller than the full MUSE field of view, was chosen to avoid issues related to the shorter exposure times experienced by the peripheral regions due to the dithering. The neutral hydrogen in the intergalactic medium is expected to suppress virtually all of the flux blueward of the Lyα line in high-redshift galaxies. We thus excluded from our analysis sources also present in the pseudo-narrowband image obtained by collapsing $DATA_{\lambda,i}$ over the wavelength slices 4750 Å–8500 Å. Finally, single-exposure datacubes were visually inspected to identify false detections associated with highly deviating pixels present in only one OB.

This procedure allowed us to reveal the presence of an LAE in the immediate proximity of J0305−3150 (R.A. = 03:05:16.80, decl. = −31:50:57.3, epoch = J2000; see Figure 8). This appears as an 8.3σ detection in the pseudo-narrowband images created by summing up slices in the $DATA_{\lambda,i}$ datacube from 9269.75 Å to 9277.25 Å, and as a 4.2σ, 3.5σ, and 5.1σ detection in the single OB datacubes collapsed in the same wavelength range (see Figure 8). Figure 9 shows the spectrum extracted over a circular aperture with a radius of 3 spaxel. By fitting a Gaussian function over the most prominent emission line, we derive a redshift of $z_{LAE} = 6.629$ (i.e., redshifted by ∼560 km s^{-1} with respect to the QSO's systemic redshift), an $FWHM_{LAE} = 240$ km s^{-1}, and a luminosity $L(\text{Ly}\alpha) = (2.1 \pm 0.2) \times 10^{42}$ erg s^{-1}. Consistently,

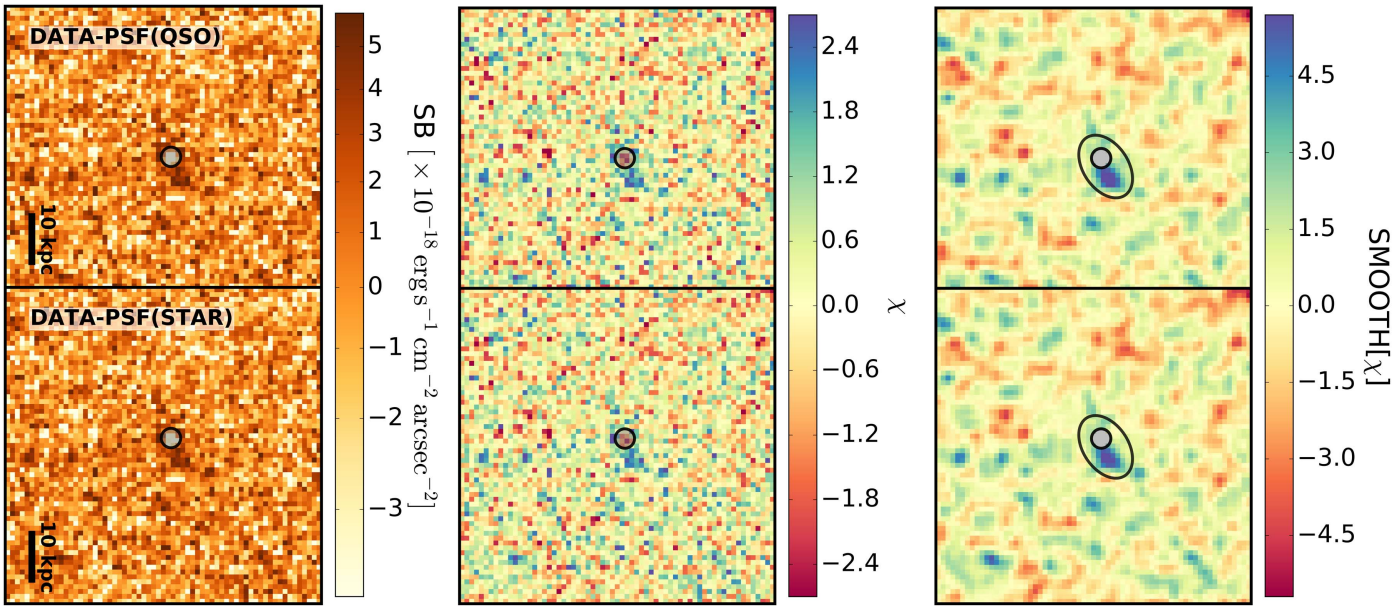

Figure 5. Result of the PSF subtraction procedure in the wavelength range where the presence of an extended Lyα halo is tentatively detected (from 9259.75 Å to 9262.25 Å, i.e., over three wavelength slices; see Figure 7). The different panels show (from left to right) DATA$_i$ − MODEL$_i$, χ_i, and SMOOTH[χ_i] pseudo-narrowband images obtained using PSF$_{\rm QSO}$ (top row) and PSF$_{\rm STAR}$ (bottom row). The size of the boxes is 13″ × 13″ (70 kpc × 70 kpc at the QSO's redshift). Images are oriented to have north on the top and east on the left. The color scale used here is the same as in Figures 2 and 3. The area used to normalize the PSF models to the QSO is marked with a black circle. This region was masked out to produce the SMOOTH[χ_i] images. The elliptical aperture used to derive the photometry of the extended emission is shown in the rightmost panels. The 5σ nominal SB limit reached in this pseudo-narrowband image is SB$^{\rm l}_{5\sigma}$ = 2.2 × 10^{-18} erg s^{-1} cm^{-2} arcsec^{-2} over a 1 arcsec^2 aperture. A significant excess of residuals is present toward the southwest considering both PSF models. We notice that our procedure slightly oversubtracts the QSO emission. The total flux coming from the putative halo could thus be underestimated.

the luminosity directly estimated from the pseudo-narrowband image is $L(\mathrm{Ly}\alpha) = (1.8 \pm 0.2) \times 10^{42}$ erg s^{-1}. No significant continuum emission is detected redward of the Lyα line.

To quantify the effect of systematics, we performed the same empirical test used in Section 3.3. From the pseudo-narrowband image, we extracted an ensemble of circular apertures with 3 spaxel radius, avoiding bright sources and image edges. The distribution of the flux over noise ratio of these apertures is well-reproduced by a Gaussian with average $\mu = 0.31$ and sigma $\sigma = 1.21$ (see Figure 10). The significance of the detection of the LAE emitter, once systematics are taken into account, is thus 6.8σ. In Figure 9, we compare the spectra extracted from the circular apertures considered above with the spectrum of the LAE. Despite the relatively low S/N per voxel of the line, seven consecutive slices have S/N > 2 and the whole emission is the brightest line detected within ±1000 km s^{-1} from the QSO's systemic redshift. These results corroborate the reliability of the LAE's detection. Given the high redshift of this source, MUSE is not able to cover additional rest-frame UV line diagnostics (e.g., He II, C IV), which would allow us to better determine the strength (and nature) of this faint companion.

5. Discussion

In the following, we discuss the implications of the tentative detection of the extended Lyα emission associated with the high-redshift QSO J0305−3150 (Sections 5.1 and 5.2) and of its companion galaxy (Section 5.3). It is worth mentioning that the real luminosity of the Lyα emission could be slightly underestimated due to the presence of neutral hydrogen in the proximity of the QSO. This effect is, however, negligible in the context of the forthcoming discussion.

5.1. The Host Galaxy of J0305−3150

In Section 3.3, we present a possible detection of extended Lyα emission around the QSO J0305−3150. The significance of this emission is strengthened by its spatial and redshift positions (close to what is expected from the [C II] emission). In this section, we link this discovery with the properties of the QSO's host galaxy.

Figure 11 maps the distribution of [C II] (as observed with ALMA) overplotted on the Lyα halo detected with MUSE. The two emissions do not appear to be co-spatial. A displacement of the Lyα and [C II]/dust emission has been commonly observed in other dusty sources at high redshift. For instance, Hodge et al. (2015) reported a ∼4 kpc offset between the rest-frame UV and both the FIR and the CO emission in the $z = 4.05$ submillimeter galaxy GN 20. Decarli et al. (2016) and Aravena et al. (2016) observed a comparable shift in the compact star-forming galaxy ASPECS C.1 ($z = 2.54$). In a similar fashion, the Lyα extended emission not associated with the radio jet, the rest-frame UV continuum, and the dust emission (albeit the coarse spatial resolution) appear to be offset in the $z = 4.11$ radio galaxy TN J1338−1942 (e.g., De Breuck et al. 2004; Zirm et al. 2005; Venemans et al. 2007; Swinbank et al. 2015).

For J0305−3150, we can estimate the obscuration due to the copious amounts of dust detected with ALMA ($M_{\rm dust}$ = (4.5–24) × 10^8 $M_\odot$; Venemans et al. 2016) by comparing the luminosity of the observed extended Lyα emission with the theoretical (unobscured) Lyα emission expected due to the UV photons coming from the intense starburst detected at millimeter

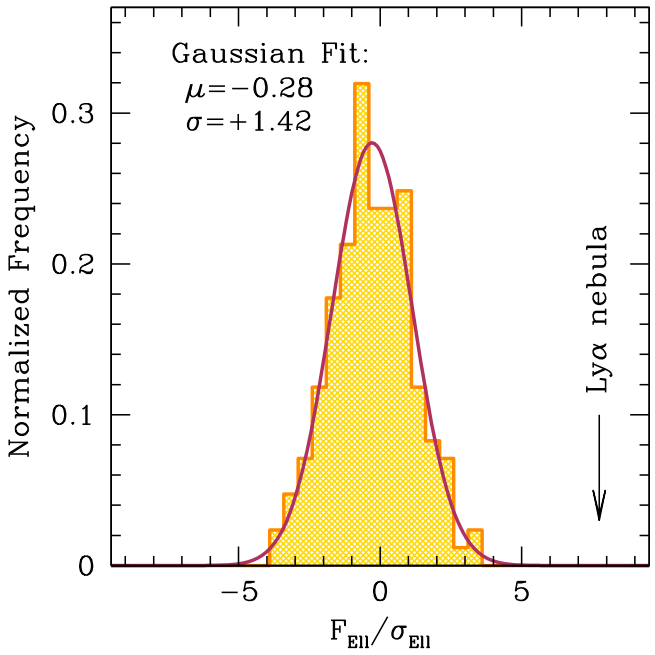

Figure 6. Analysis of the significance of the possible Lyα nebula detected in the MUSE datacube. The orange histogram is the distribution of flux over noise of the elliptical apertures, with the same extent as the one used to extract the extended emission (see Section 3.3), randomly placed in the pseudo-narrowband image obtained by collapsing $\mathrm{DATA}_i - \mathrm{MODEL}_i$ from 9259.75 Å to 9262.25 Å. The arrow marks the position of the tentatively detected halo. The Gaussian fit of the distribution (purple line) has an average of $\mu = -0.28$ and a sigma of $\sigma = 1.42$. These shifts from the expected values ($\mu = 0$, $\sigma = 1$) reflect systematics in the final datacube due, for instance, to poor sky subtraction and to correlation among voxels. Taking into account this distribution, the significance of the detection is therefore 5.1σ for $\mathrm{PSF_{QSO}}$ and 4.7σ for $\mathrm{PSF_{STAR}}$.

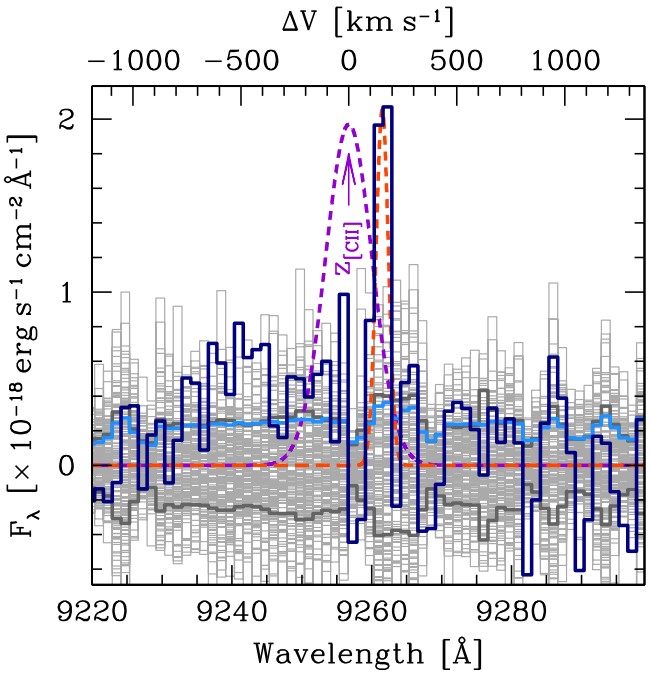

Figure 7. Spectrum of extended Lyα emission extracted over an elliptical aperture with a semiminor axis of $0\farcs9$ and semimajor axis of $1\farcs4$ in the $\mathrm{DATA}_{\lambda,i} - \mathrm{MODEL}_{\lambda,i}$ datacube (blue solid line); 1σ flux uncertainties are shown in light blue. A circle with radius $0\farcs4$ centered at the QSO position is removed before extracting the spectrum (see Figure 5). The top axis (ΔV) indicates the velocity shift with respect to the QSO's systemic redshift. As in Figure 1, the purple dashed Gaussian shows the expected position and width of the Lyα line if it is centered at z_{sys} and with an FWHM equal to the [C II] line. The possible Lyα halo appears as a bright spike at $\lambda = 9261.5$ Å. A Gaussian model of the line is shown in red. Light gray histograms are spectra randomly extracted within a radius of $25''$ from the QSO's position (see Section 3.3 for details). The 1σ dispersion of these spectra in each voxel is highlighted in dark gray. The excess of flux at ~9240 Å appears to be related to correlations present in the MUSE data and/or to non-optimal sky subtraction and is thus non-significative.

wavelengths. Assuming a case B recombination, the relation between $L(\mathrm{H}\alpha)$ and SFR (Kennicutt & Evans 2012) becomes

$$\frac{L(\mathrm{Ly}\alpha)}{10^{42}\ \mathrm{erg\ s^{-1}}} = 1.62\frac{\mathrm{SFR}}{M_\odot\ \mathrm{yr^{-1}}}. \quad (4)$$

The star-formation rate of the host galaxy ($\mathrm{SFR_{TIR}} = 545\,M_\odot\ \mathrm{yr^{-1}}$) yields a Ly$\alpha$ luminosity of $L(\mathrm{Ly}\alpha) = 8.8 \times 10^{44}$ erg s^{-1}, i.e., a factor ~300× brighter than the observed luminosity. This implies high extinction with $A_{\mathrm{UV}} \sim 6.2$ mag.

Resonance scattering may trap Lyα photons and dim the expected luminosity of the extended emission. The bouncing of Lyα photons between optically thick clouds increases the total path length traveled in the dusty medium, incrementing its extinction (see the discussion in Decarli et al. 2012 and the Appendix in Hennawi & Prochaska 2013). The relative importance of this effect strongly depends on various QSO host galaxy properties, such as neutral hydrogen column density, neutral fraction, dust-to-gas ratio, and geometry, among others. However, there is no clear evidence for a broad double-peaked kinematics as expected from resonantly trapped Lyα photons (e.g., Cantalupo et al. 2005), possibly due to absorption from neutral hydrogen in the intergalactic medium. In addition, a high level of obscuration is in contrast with the low extinction observed toward the QSO: Figure 12 plots the broadband photometry for J0305−3150 taken from Venemans et al. (2013). The SED matches well the QSO composite spectrum of Selsing et al. (2016), leaving room for only little extinction. Assuming an SMC extinction curve (Gordon et al. 2003), which is appropriate for non-BAL QSOs at high redshift (e.g., Gallerani et al. 2010), we can infer a stringent limit on the obscuration of $A_{\mathrm{UV}} < 0.1$ mag.

These results suggest that the copious amounts of dust detected with ALMA ($M_{\mathrm{dust}} = (4.5\text{–}24) \times 10^8\,M_\odot$; Venemans et al. 2016) can effectively obscure the UV emission and prevent the ionizing photons from escaping the QSO's host galaxy. However, UV radiation is able to leak through small openings in the dust cocoon. These leakages may be associated with short and extreme bursts of star formation that have been proposed to explain the intrinsically blue rest-frame UV slope observed in dusty, star-forming galaxies ($\mathrm{SFR} > 50\,M_\odot\ \mathrm{yr^{-1}}$) up to $z \sim 5$ (e.g., Casey et al. 2014). A similar scenario was also proposed by Decarli et al. (2012) to explain the lack of extended Lyα emission from the host galaxy of the two highly star-forming $z > 6$ QSOs: SDSS J1030+0524 and SDSS J1148+5251 (see also Mechtley et al. 2012).

5.2. Large-scale Lyα Emission

Is the SB limit reached with MUSE sufficient to probe the presence of Lyα nebular emission on scales of 5–100 kpc? To test this possibility, we compare our detection limits with the circularly averaged SB profiles of bright QSOs at intermediate

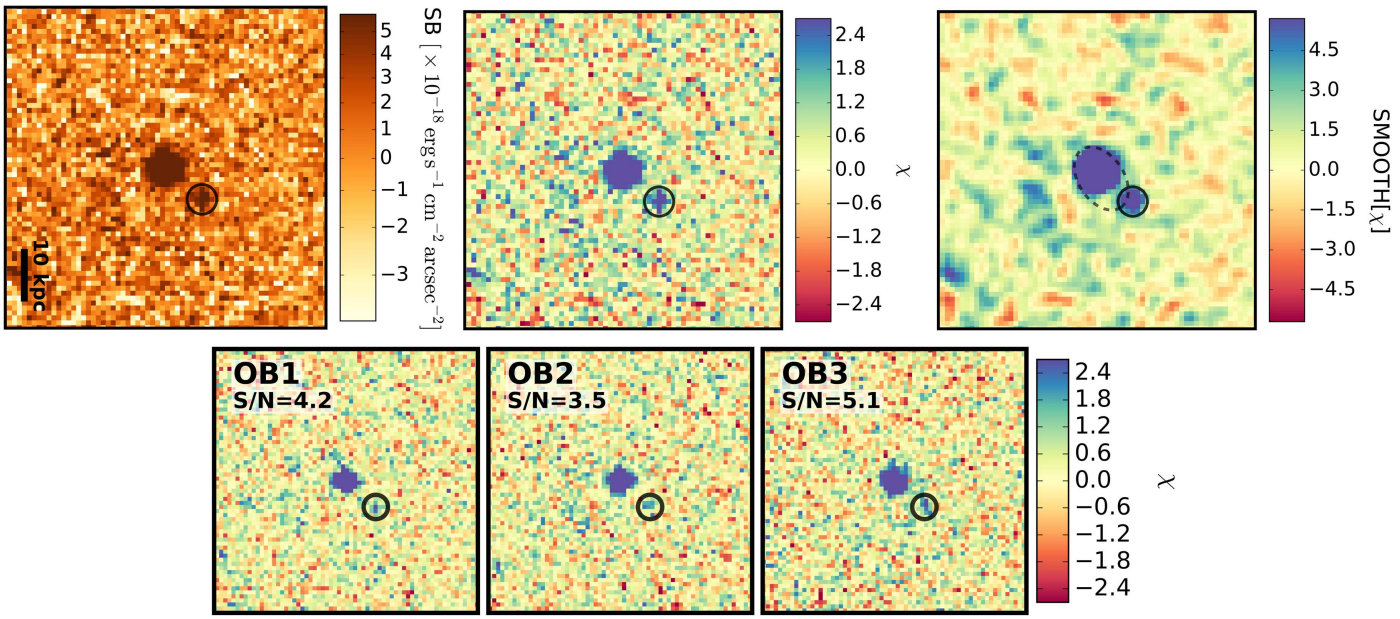

Figure 8. Detection of one LAE candidate in the proximity of J0305−3150. The different panels on the top show (from left to right) DATA$_i$, χ_i, and SMOOTH[χ_i] pseudo-narrowband images obtained by summing up the wavelength slices from 9269.75 Å to 9277.25 Å in the DATA$_{\lambda,i}$ datacube. A source (highlighted with black circles) is detected 2.″3 (∼12.5 kpc) from J0305−3150 with a formal significance of 8.3σ. The dashed ellipse marks the position where the extended Lyα halo is located (see Figure 5). On the bottom, pseudo-narrowband χ_i images obtained from the single OB exposures. The source is detected with S/N > 3 in all the images. Box sizes and color scales are the same as in Figure 5.

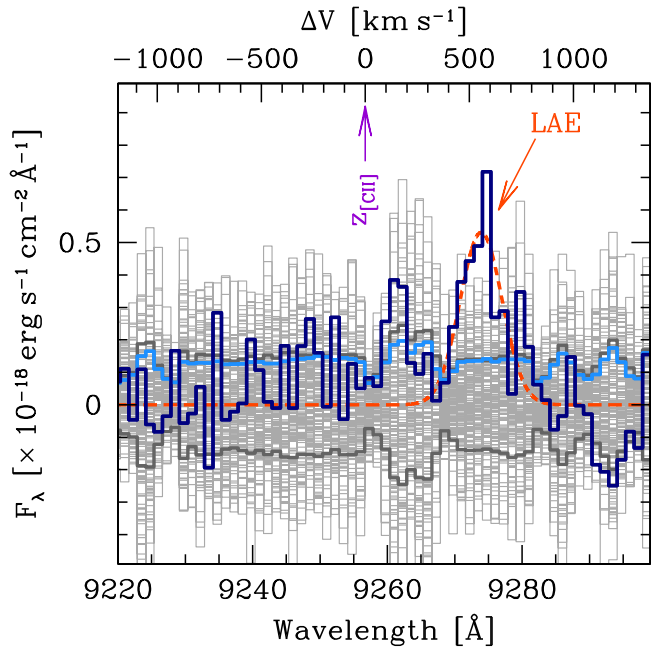

Figure 9. Spectrum of the LAE extracted over a 0.″6 circular aperture in the DATA$_{\lambda,i}$ datacube. The color code of the lines is the same as in Figure 7. The detected line is well-fitted by a Gaussian shifted 560 km s^{-1} with respect to the QSO's systemic redshift (estimated from the [C II] emission line) and with an FWHM of 240 km s^{-1}.

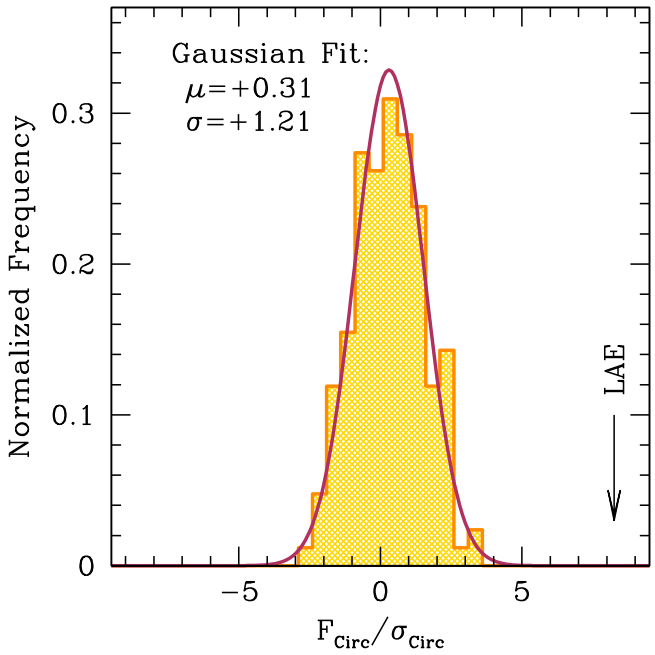

Figure 10. Analysis of the significance of the LAE detected in the MUSE datacube. The histogram is created as for Figure 6 but with a circular aperture with 0.″6 radius extracted over the collapsed DATA$_{\lambda,i}$ datacube. The Gaussian model of the distribution has $\mu = 0.31$ and $\sigma = 1.21$. Correcting for systematics, the significance of the LAE is 6.8σ.

redshift. As a comparison sample, we consider the recent work of Borisova et al. (2016a), who investigated 17 radio-quiet QSOs at $3.0 \lesssim z \lesssim 3.9$. We stress that, with a median absolute magnitude at 1450 Å of $M_{1450} = -29.2$, these are among the brightest QSOs at $z \sim 3.5$, hence they are ∼3 mag brighter than J0305−3150. The nebulae surrounding these QSOs extend on scales of 50–100 kpc and their circularly averaged SB profiles are well-represented by a power-law decline in the majority of the cases. In Figure 13, we plot the power-law best fits of these extended Lyα emissions as they would appear if moved at $z = z_{sys}$, which means we corrected for redshift dimming and for different angular diameter distances. We also

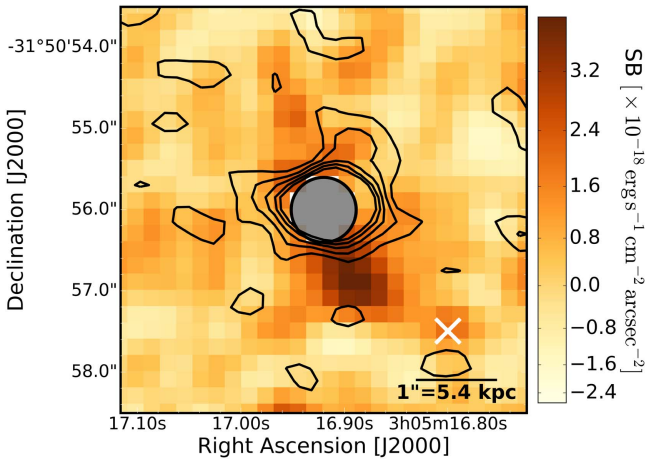

Figure 11. Comparison between the extended Lyα emission detected in the PSF-subtracted MUSE datacube (background image; see also Figure 5) and the (resolved) [C II] emission line detected with ALMA by Venemans et al. (2016; black contours). The black contours trace the [C II] line emission of J0305−3150 at the [1.5, 3.0, 4.5, 6.0, 7.5]σ significance level. The PSF-subtracted pseudo-narrowband image was convolved with a 2D Gaussian kernel with $\sigma = 1$ spaxel after removing the central region used to normalize the PSF (gray filled circle). The white cross on the bottom-right corner marks the position of the LAE detected at $z = 6.629$.

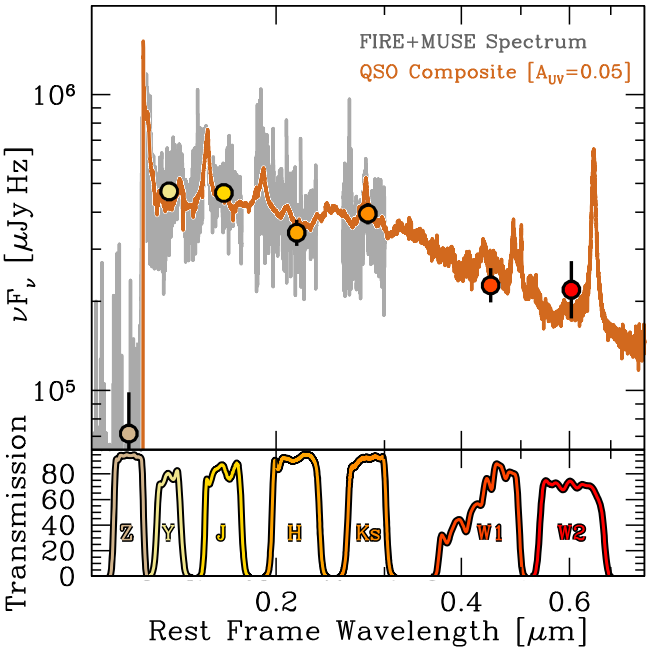

Figure 12. Top panel: SED of J0305−3150 (filled circles; see Venemans et al. 2013 for details on the photometry). The combine dFIRE+MUSE spectrum of the QSO is shown in gray (see De Rosa et al. 2014 for details). The brown spectrum is the QSO composite from Selsing et al. (2016) corrected for IGM absorption following Meiksin (2006). The normalization is set by the *W*2 photometry. A mild extinction of $A_{UV} = 0.05$ permits the photometry in the bluer bands to be matched. This implies that dust obscuration does not strongly affect the QSO emission along the line of sight. Bottom panel: transmission curves of the *Z*, *Y*, *J*, *H*, *Ks*, *W*1, and *W*2 bands used to create the SED.

show the profile of the extended Lyα emission associated with J0305−3150 averaged over annuli evenly spaced in logarithmic space together with our nominal 5σ limit on the SB. It is apparent that if J0305−3150 were surrounded by an extended emission similar to bright $z \sim 3.5$ QSOs, our MUSE data would have been deep enough to detect it at angular scales $\theta \gtrsim 1''$.

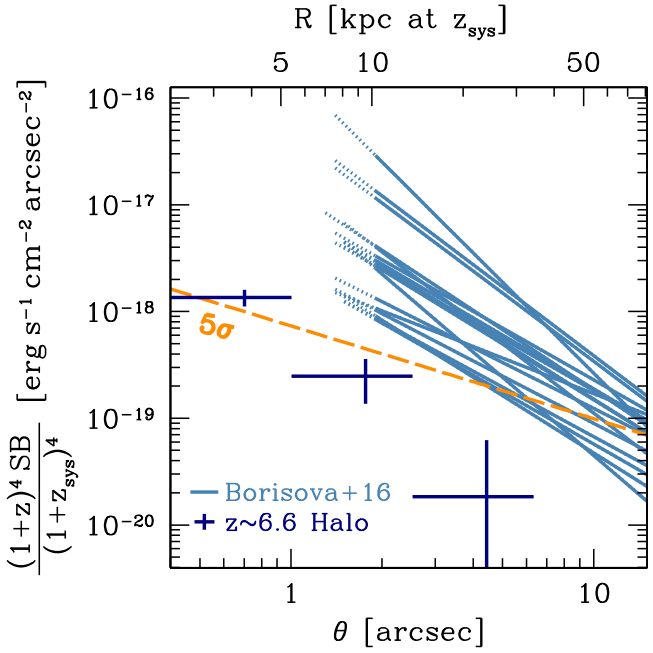

Figure 13. Redshift-corrected SB radial fit of $z \sim 3.5$ radio-quiet QSOs from Borisova et al. (2016a; light blue solid lines) compared with the nominal 5σ SB limit reached by collapsing the datacube over five wavelength slices centered at z_{sys} (orange dashed line). The power-law fits for intermediate-redshift QSOs are extrapolated down to a separation of 1″ (at the QSO's redshifts) where no information on the extended emission could be provided due to the PSF subtraction procedure (light blue dotted lines; see Borisova et al. 2016a for details). The circularly averaged profile of emission around J0305−3150 is also shown for comparison (dark blue crosses). This profile is calculated in annuli with radii evenly spaced in logarithmic space. Despite its asymmetric morphology, the tentative extended emission is detected just above the 5σ level in the inner 0.″4–1.″0 annulus.

The nebular emission around J0305−3150 appears to have a significantly lower SB and lower total luminosity than commonly observed at intermediate redshifts. In Figure 14, we present a compilation of Lyα nebulae detected around QSOs from the literature.[12] The 5σ upper limits on the luminosity set by Decarli et al. (2012) on SDSS J1030+0524 ($z = 6.31$) and SDSS J1148+5251 ($z = 6.42$) are also plotted. These are derived by rescaling their 5σ SB limit ($SB^{1}_{5\sigma} = 1.0 \times 10^{-17}$ erg s^{-1} cm^{-2} arcsec^{-2} over a 1 arcsec^2 aperture) to a circular aperture with a diameter of 10 kpc. On the right side of Figure 14, we mark the 5σ upper limits on the luminosity for top-hat sources with diameters $d = [10, 25, 50, 100]$ kpc and FWHM $= 200$ km s^{-1}. These are calculated considering the SB limit obtained by collapsing the MUSE datacube over five wavelength slices ($SB^{1}_{5\sigma,\lambda} = 1.9 \times 10^{-18}$ erg s^{-1} cm^{-2} arcsec^{-2} over a 1 arcsec^2 aperture; see Section 3.2). These data suggest a decline in the total luminosity of the Lyα nebulae as a function of redshift. This may indicate a change in the gas properties and/or in the powering mechanisms at different epochs. A more quantitative interpretation, however, is hampered by the differing

[12] Data are from Heckman et al. (1991a, 1991b), Bremer et al. (1992), Roettgering et al. (1997), van Ojik et al. (1997), Lehnert & Becker (1998), Bergeron et al. (1999), Fynbo et al. (2000), Bunker et al. (2003), Weidinger et al. (2004), Weidinger et al. (2005), Christensen et al. (2006), Courbin et al. (2008), Barrio et al. (2008), Yang et al. (2009), Smith et al. (2009), Matsuda et al. (2011), Willott et al. (2011), North et al. (2012), Humphrey et al. (2013), Cantalupo et al. (2014), Roche et al. (2014), Husband et al. (2015), Hennawi et al. (2015), Borisova et al. (2016a), Fumagalli et al. (2016), and Fathivavsari et al. (2016). Effects of different sensitivities are not taken into account.

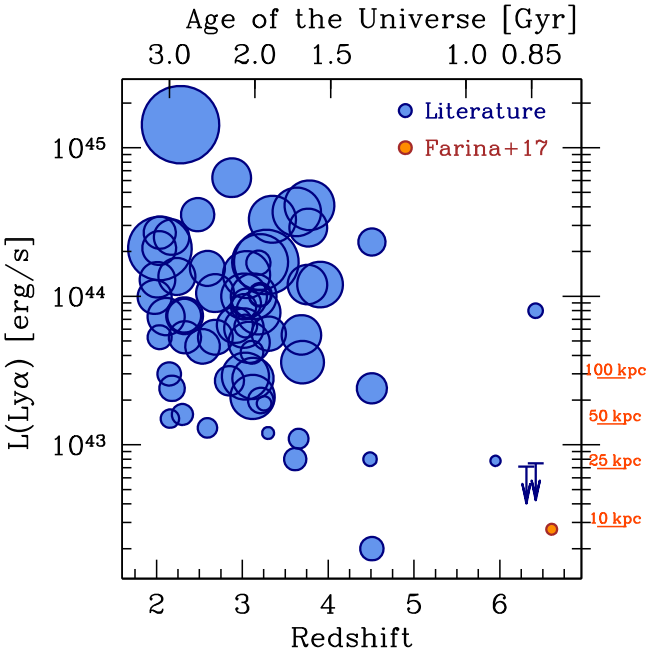

Figure 14. Distribution of all Lyα nebulae associated with QSOs known to date in the redshift vs. total Lyα luminosity plane (blue circles). The radius of the points is proportional to the square root of the maximum extent of the Lyα emissions. Data at $z > 5$ are SDSS J2228+0110 ($z = 5.95$; Roche et al. 2014) and CFHQS J2329−0301 ($z = 6.42$; Willott et al. 2011) The arrows are the 5σ upper limits set by Decarli et al. (2012) on SDSS J1030+0524 ($z = 6.31$) and SDSS J1148+5251 ($z = 6.42$; see the text for details). The extended emission associated with J0305−3150 is plotted as an orange filled circle. Ticks on the right side of the plot mark nominal sensitivity limits reached in the MUSE data calculated assuming $SB^{1}_{5\sigma} = 1.9 \times 10^{-18}$ erg s^{-1} cm^{-2} arcsec^{-2} over a 1 arcsec^2 aperture (obtained by collapsing the cube over five wavelength slices; see Section 3.2) and top-hat sources with diameters 10, 25, 50, and 100 kpc and an FWHM of 200 km s^{-1}.

methodologies, ambiguities in detection criteria, and lack of a statistical sample of QSOs investigated at $z > 4$.

It is of interest to compare our observational results with predictions on the luminosity of the Lyα for different emission mechanisms. In Section 5.2.1, we consider the case of recombination from optically thick clouds. The case in which the QSO radiation highly ionizes the surrounding gas which thus becomes optically thin is addressed in Section 5.2.2. Finally, in Section 5.2.3, we comment on the possibility that the gas is in a multiphase status. These calculations closely follow the formalism described in Hennawi & Prochaska (2013).

5.2.1. Optically Thick Gas

Under the assumption that the surrounding of the QSO is filled with cool, optically thick clouds, self-shielding generates a thin, highly ionized envelope around individual clouds that acts as a mirror converting a fraction of the ionizing radiation into Lyα photons (Gould & Weinberg 1996). In this scenario, the powering mechanism is the QSO ionizing radiation ($L_{\nu_{\rm LL}}$, where $\nu_{\rm LL}$ is the frequency at the Lyman edge). L(Lyα) is thus proportional to $L_{\nu_{\rm LL}}$ as

$$\frac{L({\rm Ly}\alpha)}{10^{44}\ {\rm erg\ s^{-1}}} = 7.8\, f_c^{\rm thick} \frac{L_{\nu_{\rm LL}}}{10^{30}\ {\rm erg\ s^{-1}\ Hz^{-1}}}, \quad (5)$$

where $f_c^{\rm thick}$ is the optically thick cloud-covering factor. If we assume $f_c^{\rm thick} = 0.1$ as estimated for the small-scale Lyα emission observed in $z = 2$–3 QSOs by Hennawi & Prochaska (2013) and $L_{\nu_{\rm LL}} = 4.9 \times 10^{30}$ erg s^{-1} Hz^{-1} (obtained by rescaling the composite spectrum from Lusso et al. 2015 to the QSO luminosity at 1350 Å), we obtain L(Lyα) $= 3.8 \times 10^{44}$ erg s^{-1}. This discrepancy of a factor ∼130× with respect to the observed luminosity may be due to the geometry of the emission: if the UV photons break only through a small solid angle $\Omega_{\rm e}$, the expected Lyα luminosity would be reduced by a factor $f_{\Omega_{\rm e}} = \left(\frac{\Omega_{\rm e}}{4\pi}\right)$. Assuming, for the sake of simplicity, that the anisotropic emission occurs in a cone, an opening angle of 30° corresponds to $f_{\Omega_{\rm e}} \sim 0.07$. However, this would imply an unrealistic fraction of obscured AGNs of $f_{\rm Obs} = \left(1 - \frac{\Omega_{\rm e}}{4\pi}\right) = 0.85$ (e.g., Treister et al. 2008; Lusso et al. 2013; Merloni et al. 2014). Alternatively, a factor of 100× lower optically thick cloud-covering fraction may explain the faintness of the emission. Such a low covering fraction, however, is in contrast with results from $z \sim 2$ to 3 QSOs (Prochaska et al. 2013a; see also Section 5.2.3). This result pushes for different emission mechanisms to explain the observed emission.

5.2.2. Optically Thin Gas

If the gas surrounding the QSO is optically thin, the QSO radiation would be sufficiently intense to keep the gas highly ionized (i.e., the hydrogen neutral fraction is $x_{\rm H\,I} = \frac{n_{\rm H\,I}}{n_{\rm H}} \ll 1$). As shown in Hennawi & Prochaska (2013), in the optically thin regime, L(Lyα) can be expressed in terms of the area-averaged neutral column density ($\langle N_{\rm H\,I}\rangle$) and of the ionizing luminosity,

$$\frac{L({\rm Ly}\alpha)}{10^{44}\ {\rm erg\ s^{-1}}} = 0.9 \frac{\langle N_{\rm H\,I}\rangle}{10^{17.2}\ {\rm cm^{-2}}} \frac{L_{\nu_{\rm LL}}}{10^{30}\ {\rm erg\ s^{-1}\ Hz^{-1}}}, \quad (6)$$

where the normalization of $\langle N_{\rm H\,I}\rangle$ is set by the requirement that, to be optically thin, clouds must have $N_{\rm H\,I} \ll 10^{17.2}$ cm^{-2}. Plugging into this equation the observed luminosity of the nebula and the $L_{\nu_{\rm LL}}$ estimated above, we obtain $\langle N_{\rm H\,I}\rangle \sim 10^{15.0}$ cm^{-2}. It is thus plausible that the extended emission arises from optically thin clouds illuminated by the QSO. However, it is worth a reminder that while $\langle N_{\rm H\,I}\rangle > 10^{17.2}$ cm^{-2} implies that the gas is in the optically thick regime, clouds with $\langle N_{\rm H\,I}\rangle < 10^{17.2}$ cm^{-2} could be either optically thin or optically thick (see Hennawi & Prochaska 2013).

If we assume an optically thin scenario, we can relate the observed Lyα SB to the hydrogen total column density ($N_{\rm H}$) and volume density ($n_{\rm H}$; e.g., Hennawi & Prochaska 2013),

$$\frac{{\rm SB(Ly}\alpha)}{10^{-19}\ {\rm erg\ s^{-1}\ cm^{-2}\ arcsec^{-2}}} = 5.9\left(\frac{1+z}{7.6145}\right)^{-4} \times f_c^{\rm thin}\left(\frac{n_{\rm H}}{1.0\ {\rm cm^{-3}}}\right)\left(\frac{N_{\rm H}}{10^{20.5}\ {\rm cm^{-2}}}\right), \quad (7)$$

where $f_c^{\rm thin}$ is the covering fraction of the optically thin gas. From this equation, we can derive an estimate of the volume density of the gas giving rise to the extended emission. In fact, the total column density of the hydrogen in the proximity of $z \sim 2$ QSOs has been constrained from the study of absorption systems. Photoionization models of these absorbers suggest that $N_{\rm H}$ is almost constant within an impact parameter of

200 kpc with a median value $N_{\rm H} = 10^{20.5}\,{\rm cm}^{-2}$ (e.g., Prochaska & Hennawi 2009; Hennawi et al. 2015; Lau et al. 2016). Assuming $f_c^{\rm thin} = 0.5$, to explain the observed SB SB(Lyα) = $(1.8 \pm 0.2) \times 10^{-18}$ erg s^{-1} cm^{-2} arcsec^{-2} (calculated over the elliptical aperture considered in Section 3.3), a high gas volume density of $n_{\rm H} = 6.1\,{\rm cm}^{-3}$ is required. Remarkably, similarly high $n_{\rm H}$ were proposed to explain the emission of the giant Lyα nebulae associated with the QSOs UM 287 (Cantalupo et al. 2014; Arrigoni Battaia et al. 2015b) and SDSS J0841+3921 (Hennawi et al. 2015).

5.2.3. A Multiphase Scenario

In the previous sections, we estimated the expected emission from the gas surrounding J0305−3150 considering that it is either optically thick or optically thin to QSO radiation. However, we can also consider a multiphase scenario where low-density clouds with a high covering fraction are responsible for the absorption systems observed at $z \sim 2$, whereas the observed emission rises from optically thick gas with a low covering fraction (and hence rarely intercepted in absorption). We also stress that disentangling the different emission mechanism is challenging. At a given separation from the QSO, optically thick and optically thin gas clouds could result in a similar emission with opportune combinations of $n_{\rm H}$, $N_{\rm H}$, and covering fraction. From Equations (6) and (7), it is clear that, for a given $N_{\rm H}$, one can consider increasing $n_{\rm H}$ to increase the emission in the optically thin regime. However, when the area-averaged neutral column density reaches $\langle N_{\rm H\,I}\rangle \sim 10^{17.2}\,{\rm cm}^{-2}$, the cloud becomes optically thick and recombination would occur only in the self-shielding layer. We can thus roughly calculate the density required for a cloud to become optically thick as a function of the distance from the QSO by matching the emission estimates in Sections 5.2.1 and 5.2.2 (for the same covering factor). We obtain that, in order to shelf-shield at a separation of 25 kpc from J0305−3150, a cloud should have a high density of $n_{\rm H} \sim 200\,{\rm cm}^{-3}$.

5.3. Overdensity of LAEs around the J0305−3150

The first search for LAEs around $z > 5.5$ QSOs was performed by Decarli et al. (2012) using a combination of narrowband filters of the WFC3 on *HST*. No companion galaxies were found around the two QSOs SDSS J1030+0524 and SDSS J1148+5251. However, the field of view of WFC3 allowed the authors to probe only a small cosmological volume and a relatively bright point source detection limit was reached (∼23.4 mag). Bañados et al. (2013) and Mazzucchelli et al. (2017b) used sensitive narrow- and broadband images from the FOcal Reducer/low dispersion Spectrograph 2 (FORS2) on the VLT to investigate the environment of the two QSOs ULAS J0203+0012 ($z = 5.72$) and PSO J215.1512−16.0417 ($z = 5.73$) over a much larger area (∼37 arcmin^2). Both studies report a number of LAEs consistent with (or even lower than) expectations from a blank field. Goto et al. (2017), using the Subaru Prime Focus Camera (Suprime-cam) on the Subaru telescope, similarly reported an underdensity of LAEs around the QSO CFHQS J2329−0301 ($z = 6.4$). It is worth mentioning that at slightly lower redshift, McGreer et al. (2014) discovered an LAE in the immediate proximity (with a separation of only 11.4 kpc) of the $z \sim 4.9$ QSO SDSS J0256+0019.

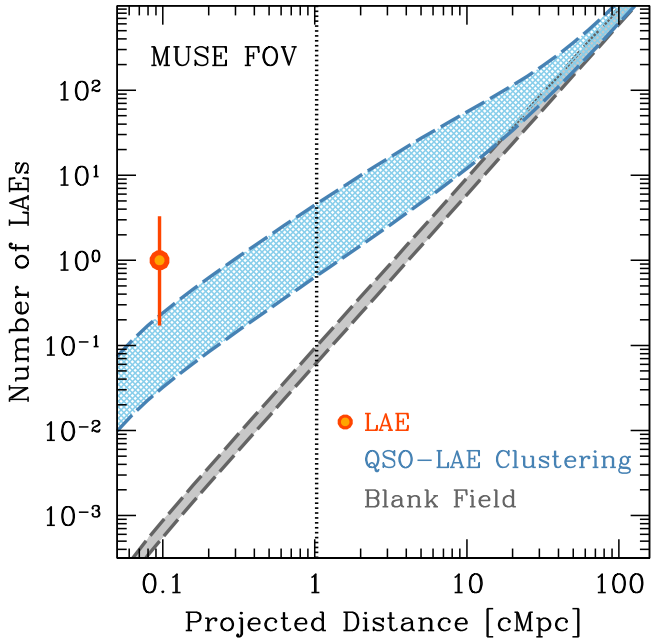

Figure 15. Number density of LAEs as a function of projected distance. The gray shaded area shows the expected number of LAEs located within ±1000 km s^{-1} from the QSO systemic redshift. This is obtained by integrating the $z \sim 6.6$ LAE luminosity function of Matthee et al. (2015) down to the 5σ luminosity limit reached by our observations (i.e., $L_{5\sigma} = 10^{41.8}$ erg s^{-1}). In the absence of clustering, the LAE detected at a projected distance of 12.5 kpc from J0305−3150 (orange point; error bars are the 1σ confidence interval derived following Gehrels 1986) appears to be a factor ∼1000× above expectations. The large-scale QSO–LAE clustering (see Section 5.3) increases the expected number of LAEs in the proximity of a QSO (blue shaded area). Even considering the upper limit on the $z \sim 6.6$ LAE–LAE auto-correlation function to determine the QSO–LAE cross-correlation length, fewer than ∼0.1 LAEs are expected at separations <15 kpc.

The detection of one LAE in the MUSE datacube at only ∼12.5 kpc and 560 km s^{-1} from J0305−3150 may represent the first spectroscopically confirmed evidence of the connection between high-density environments (and thus high merger rate) and $z > 6$ QSOs, which was postulated to explain the rapid assembly of the first SMBHs (e.g., Volonteri 2012). To confirm this scenario, we have to calculate first the probability of finding such LAEs in the proximity of the QSO.

5.3.1. Comparison to Blank Field

In order to estimate how many LAEs are expected from the blank field, we integrated the $z \sim 6.6$ LAE luminosity function from Matthee et al. (2015)[13] down to our 5σ luminosity limit for an unresolved source (i.e., $L_{5\sigma} = 6.7 \times 10^{42}$ erg s^{-1}; see Section 4). The derived number density of LAEs is $\phi(L > 10^{41.8}\,{\rm erg\,s^{-1}}) = (5.8^{+1.9}_{-1.2}) \times 10^{-4}\,{\rm cMpc^{-3}}$. This means that ≲0.1 LAEs are expected within the total volume explored in our analysis (i.e., 50″ × 50″ × 2000 km s^{-1} or ∼80 cMpc^3; see Section 4) and a mere $\sim 10^{-3}$ within a separation of 12.5 kpc (see Figure 15). Such a low incidence of LAEs due to the blank field supports the idea that the detected LAE has to be physically linked to the presence of the QSO.

[13] As suggested in Matthee et al. (2015), we conservatively consider the fit of the spectroscopically confirmed UDS+COSMOS sources with a fixed faint-end slope $\alpha = -1.5$.

5.3.2. Comparison to QSO–LAE Clustering

The study of the QSO–galaxy and QSO–QSO clustering showed that bright QSOs at low and intermediate redshifts are biased tracers of massive dark matter halos with $M_{\rm DM} \gtrsim 10^{12.5}\,M_{\odot}$ (e.g., Myers et al. 2007; Shen et al. 2007; Padmanabhan et al. 2009; Ross et al. 2009; Farina et al. 2011; Richardson et al. 2012; White et al. 2012; Shen et al. 2013; Zhang et al. 2013; Karhunen et al. 2014; Sandrinelli et al. 2014; Eftekharzadeh et al. 2015, 2017; Garcia-Vergara et al. 2017). At high redshift, constraints are given by the discovery of a QSO pair with a projected separation of only 130 kpc at $z = 5.02$ (McGreer et al. 2016). The inferred correlation length is $r_0 > 29$ cMpc, which is consistent with the $r_0 \sim 30$ cMpc estimated by Shen et al. (2007, 2010) from a sample of QSO pairs at $3.5 < z < 4.5$. To predict the expected number of LAEs in the presence of clustering, we follow the formalism proposed by Hennawi et al. (2006b). In summary, the real space two-point QSO–LAE cross-correlation function $\xi^{\rm QG}$ is integrated along the line of sight to eliminate distance distortions in redshift space, and the expected number of companions is calculated in cylindrical shells ($V_{\rm shell}$) centered on the QSO. In practice, $\xi_{\rm QG}$ can be expressed as

$$\xi^{\rm QG}(r, R) = \left[\frac{(r^2 + R^2)^{\frac{1}{2}}}{r_0^{\rm QG}}\right]^{-\gamma}, \quad (8)$$

where r and R are comoving coordinates, perpendicular to and along the line of sight, respectively; $r_0^{\rm QG}$ is the QSO–LAE cross-correlation length; and γ is the slope of the correlation function (e.g., Peebles 1980). In the presence of clustering, the number of LAEs expected within a cylindrical shell of volume $V_{\rm shell}(r) = \pi(r^2 - r_{\rm min}^2)\,\Delta R$, where $r_{\rm min}$ is the minimum radius (in comoving Mpc) that can be probed in the MUSE datacube (i.e., the seeing radius), r is the comoving transverse distance from the QSO, and ΔR is the comoving line-of-sight distance corresponding to the velocity range $\pm 1000\,{\rm km\,s^{-1}}$ from the QSO's systemic redshift, is

$$N_{\rm C}(L_{\rm Lim}, r) = \phi(L_{\rm Lim})\,V_{\rm shell}(r)[1 + \bar{W}_p^{\rm QG}(r_{\rm min}, r)], \quad (9)$$

where the volume-averaged projected cross-correlation function ($\bar{W}_p^{\rm QG}$) is given by

$$\bar{W}_p^{\rm QG}(r_{\rm min}, r) = \frac{\int_{-\frac{\Delta R}{2}}^{+\frac{\Delta R}{2}} dR' \int_{r_{\rm min}}^{r} 2\pi r' dr' \xi^{\rm QG}(r', R')}{V_{\rm shell}(r)}. \quad (10)$$

To infer $r_0^{\rm QG}$, we consider that, by definition, $\xi_{\rm QG}$ could be expressed as

$$\xi^{\rm QG}(r, R) = \langle \delta_{\rm Q}(r, R)\delta_{\rm G}(r, R)\rangle, \quad (11)$$

where $\delta_{\rm Q}$ and $\delta_{\rm G}$ are the relative density contrasts of QSOs and LAEs, respectively, and the angular brackets denote averaging over a distribution. Under the assumption that QSOs and LAEs trace the same underlying dark matter distribution and considering a linear bias ($\delta_{\rm Q} = b_{\rm Q}\delta_{\rm DM}$ and $\delta_{\rm G} = b_{\rm G}\delta_{\rm DM}$), Equation (11) can be rewritten as

$$\xi^{\rm QG}(s, R) = b_{\rm Q} b_{\rm G} \xi^{\rm DMDM}(r, R) = [\xi^{\rm QQ}(r, R)\xi^{\rm GG}(r, R)]^{\frac{1}{2}}, \quad (12)$$

where $\xi^{\rm DMDM}$, $\xi^{\rm QQ}$, and $\xi^{\rm GG}$ are the real space two-point auto-correlation functions for dark matter halos, QSOs, and LAEs, respectively (e.g., Schneider 2006). Assuming a power-law form for both $\xi^{\rm QQ}$ and $\xi^{\rm GG}$ (with the same γ), the QSO–LAE cross-correlation length could be estimated as

$$r_0^{\rm QG} = (r_0^{\rm QQ} r_0^{\rm GG})^{\frac{1}{2}}, \quad (13)$$

where $r_0^{\rm QQ}$ and $r_0^{\rm GG}$ are the QSO–QSO and LAE–LAE auto-correlation lengths. As a proxy for $r_0^{\rm QG}$ at $z \sim 6.6$, we considered $r_0^{\rm GG} = 10.3^{+4.7}_{-8.6}$ cMpc, which is the upper limit on the auto-correlation length derived by Ouchi et al. (2010) from the clustering analysis of bright LAEs at $z = 6.6$ and $r_0^{\rm QQ} = 17.4^{+2.5}_{-2.8}$ cMpc obtained by imposing $\gamma = 1.8$ on the study of the clustering properties of $z > 2.9$ QSOs of Shen et al. (2007). It is worth noticing that, at $z \sim 1$–2, the QSO–QSO auto-correlation function appears to get steeper at sub-Mpc separations (e.g., Djorgovski 1991; Hennawi et al. 2006; Djorgovski et al. 2007; Myers et al. 2007, 2008; Hennawi et al. 2010; Kayo & Oguri 2012; Farina et al. 2013). However, this enhancement becomes less prominent at $z > 2.9$ where small- and large-scale clustering amplitudes are comparable (Shen et al. 2010).

Figure 15 shows, as a function of r, the estimated number of LAEs located within $\pm 1000\,{\rm km\,s^{-1}}$ from the QSO's systemic redshift. Considering the cross-correlation length estimated above, $\lesssim$0.1 LAEs are expected within 100 ckpc from the QSO. The presence of one LAE with such a small separation suggests a physical interaction with the QSO's host galaxy. Intriguingly, the detected LAE and the possible Lyα halo point to each other both in velocity and in position with respect to the QSO, opening up the possibility that we may be witnessing an ongoing merger and that the Lyα halo may be associated with the interaction between the LAE and the QSO's host galaxy. We are cautious, however, that these results are based on the detection of a single LAE in the proximity of one $z \sim 6.6$ QSO. Previous studies (Decarli et al. 2012; Bañados et al. 2013; Mazzucchelli et al. 2017b; Goto et al. 2017), even if subjected to larger redshift uncertainties, did not report any evidence for an excess of LAEs in the proximity of $z \sim 6$ QSOs (but see Decarli et al. 2017 for the detection of [C II] bright galaxies in the proximity of $z \sim 6$ QSOs). Measurements of the high-redshift QSO–galaxy clustering in a statistical fashion is thus fundamental to discern among different scenarios proposed to explain the rapid formation of SMBHs at the end of cosmic reionization.

5.3.3. Physical Properties of the LAE

The Lyα emission of the companion galaxy could be boosted by the local enhancement of the ionizing background in the vicinity of a QSO. Star formation can power the Lyα emission up to a rest-frame equivalent width of $W_0({\rm Ly}\alpha) = 240$ Å (e.g., Schaerer 2002). This value is commonly used as a limit to identify LAEs associated with a fluorescent reprocessing of QSO radiation (e.g., Cantalupo et al. 2012). Some authors consider a less stringent limit of $W_0({\rm Ly}\alpha) > 100$ Å for their selection (e.g., Trainor & Steidel 2013; Borisova et al. 2016b). However, this may lead to a high level of contamination from non-fluorescent objects (e.g., Borisova et al. 2016b).

Here, we test if the properties of the identified LAEs are consistent with a Lyα fluorescence scenario. No significant continuum emission is detected redward of the Lyα emission. To constrain W_0(Lyα), we thus consider the 1σ limit on the mean continuum (σ_C) obtained by averaging down the errors on the extracted spectrum ($\sigma_{\mathrm{LAE},\lambda}$) over the wavelength range between 9281 Å and 9350 Å (i.e., up to the edge of the datacube): $\sigma_C^2 = \sum_{\lambda=9281\text{Å}}^{9350\text{Å}} 1/\sigma_{\mathrm{LAE},\lambda}^2$. This leads to a 3σ lower limit on the rest-frame equivalent width of $W_{3\sigma}(\mathrm{Ly}\alpha) = \frac{F(\mathrm{Ly}\alpha)}{3\,\sigma_C(1+z_{\mathrm{LAE}})} = 7.4$ Å, which is not strict enough to rule out a non-fluorescent scenario. As a matter of fact, if powered by fluorescence, the luminosity of the LAE is proportional to $L_{\nu_{\mathrm{LL}}}$ and inversely proportional to the square of the perpendicular distance from the QSO, assuming, for the sake of simplicity, that the line-of-sight separation is negligible (see Hennawi & Prochaska 2013). We would expect $L(\mathrm{Ly}\alpha) \sim 7 \times 10^{43}$ erg s^{-1}, where we considered the LAE to be unresolved, i.e., with a diameter matching the seeing FWHM (0.″58). The observed luminosity is a factor ∼30× fainter. Note that this estimate depends on unknown quantities, namely, the real distance of the QSO, the luminosity of the QSO in the direction of the LAE, and the size of the surface illuminated by the ionizing radiation. These could contribute to reduce the expected fluorescence emission. On the other hand, it is possible that we are underestimating the real Lyα luminosity. Up to 90% of the flux may come from an undetected extended component (Wisotzki et al. 2016) and a fraction of the Lyα emission could be concealed by the neutral hydrogen. Within these uncertainties, we favor a scenario where star formation, rather than fluorescence, is inducing the Lyα emission. From Equation (4), we can thus derive the star-formation rate of the LAE, $\mathrm{SFR}_{\mathrm{LAE}} \sim 1.3\,M_\odot\,\mathrm{yr}^{-1}$ (see discussion in Rauch et al. 2013 for the possibility of QSO feedback triggering the star formation in a close-by LAE at $z \sim 3.0$).

6. Summary and Conclusions

In this paper, we presented a sensitive search for extended Lyα emission around the starbursting QSO J0305−3150 at $z \sim 6.61$. The nominal 5σ SB limit reached with MUSE is $\mathrm{SB}^{\mathrm{I}}_{5\sigma} = 1.9 \times 10^{-18}$ erg s^{-1} cm^{-2} arcsec^{-2} over a 1 arcsec^2 aperture (estimated by collapsing the datacube over five wavelength slices centered at $\lambda = 9256$ Å). This formally corresponds to a luminosity limit of $L_{5\sigma} \sim 10^{42.0}$ erg s^{-1} for unresolved sources with FWHM = 200 km s^{-1}, and to $L_{5\sigma} \sim 10^{43.2}$ erg s^{-1} for a circular source with a diameter of 50 kpc and the same FWHM. The primary results of this study are:

1. After carefully subtracting the unresolved emission from the central QSO, we detect the presence of a tenuous ($L(\mathrm{Ly}\alpha) = (3.0 \pm 0.4) \times 10^{42}$ erg s^{-1}) Lyα halo extending over ∼10 kpc. To date, this is the first such nebula observed at $z > 6.5$ and one of the faintest extended emissions ever observed around a QSO at any redshift (see Figure 14). Despite the depth of our data, we do not detect the large-scale (10–100 kpc) Lyα emission frequently observed in $z \sim 2$–4 bright QSOs.
2. A comparison between the Lyα emission revealed by MUSE and the FIR properties of the host galaxy inferred from ALMA observations allows us to speculate on the geometry of the dust surrounding the QSO. In particular, a patchy geometry of the dust cocoon can explain (i) the displacement between extended Lyα and resolved [C II] emission lines, (ii) the discrepancy between the observed Lyα luminosity and expectation from the intense star formation of the host galaxy, and (iii) the mild dust extinction present along the QSO line of sight. This configuration permits the ionizing radiation from the newly formed stars to escape the host galaxy and give rise to the observed Lyα emission.
3. We estimate that the extended Lyα emission is too faint to arise from recombinations on the "skin" of optically thick clouds. A more plausible scenario is that the QSO radiation is sufficiently intense to maintain the surrounding gas highly ionized, hence we are observing fluorescent emission coming from optically thin clouds. Intriguingly, a consequence of this emission mechanism is a hydrogen volume density of the gas illuminated by the QSO of $n_{\mathrm{H}} \sim 6$ cm^{-3}, similar to that estimated for the giant (≫100 kpc) Lyα nebulae recently discovered around $z \sim 2$ QSOs.
4. An LAE with $L(\mathrm{Ly}\alpha) \sim 2.1 \times 10^{42}$ erg s^{-1} is present at 12.5 kpc and 560 km s^{-1} from J0305−3150. Our current constraints on the rest-frame equivalent width ($W_0(\mathrm{Ly}\alpha) > 7.4$ Å) and luminosity, although not conclusive, disfavor a picture where the Lyα emission is boosted by the QSO radiation. Assuming that the Lyα line is powered solely by star formation, we derive a star-formation rate of $\mathrm{SFR}_{\mathrm{LAE}} \sim 1.3\,M_\odot\,\mathrm{yr}^{-1}$.
5. We calculate the enhanced probability of finding such a close LAE due to the clustering of galaxies around QSOs. From the extrapolation of the $z \sim 6.6$ QSO–LAE large-scale correlation function, we estimate this probability to be small (<10%). This supports a picture in which dissipative interaction and QSO activity in the young universe are connected.

E.P.F., B.P.V., and F.W. acknowledge funding through the ERC grant "Cosmic Dawn." Support for R.D. was provided by the DFG priority program 1573 "The physics of the interstellar medium." S.C. gratefully acknowledges support from Swiss National Science Foundation grant PP00P2_163824. E.P.F. is grateful to M. Fouesneau for providing support in the use of Python for the analysis of the MUSE datacubes, to M. Fumagalli for sharing data on the QSO Q0956+122, and to M. Rauch for providing feedback on the manuscript. We thank the members of the ENIGMA group[14] at the Max Planck Institute for Astronomy (MPIA) for helpful discussions. This research made use of Astropy, a community-developed core Python package for Astronomy (Astropy Collaboration et al. 2013); APLpy,[15] an open-source plotting package for Python based on Matplotlib (Hunter 2007); and IRAF.[16] Based on observations collected at the European Organisation for Astronomical Research in the Southern Hemisphere under ESO programme 094.B-0893(A).

ORCID iDs

Emanuele P. Farina https://orcid.org/0000-0002-6822-2254
Bram P. Venemans https://orcid.org/0000-0001-9024-8322
Roberto Decarli https://orcid.org/0000-0002-2662-8803
Joseph F. Hennawi https://orcid.org/0000-0002-7054-4332
Fabian Walter https://orcid.org/0000-0003-4793-7880

[14] http://enigma.physics.ucsb.edu/
[15] http://aplpy.github.io/
[16] IRAF (Tody 1986, 1993) is distributed by the National Optical Astronomy Observatories, which are operated by the Association of Universities for Research in Astronomy, Inc., under cooperative agreement with the National Science Foundation.

Eduardo Bañados https://orcid.org/0000-0002-2931-7824
Chiara Mazzucchelli https://orcid.org/0000-0002-5941-5214
Fabrizio Arrigoni-Battaia https://orcid.org/0000-0002-4770-6137
Ian D. McGreer https://orcid.org/0000-0002-3461-5228

References

Alam, S. M. K., & Miralda-Escudé, J. 2002, ApJ, 568, 576
Aravena, M., Decarli, R., Walter, F., et al. 2016, ApJ, 833, 71
Arrigoni Battaia, F., Hennawi, J. F., Cantalupo, S., & Prochaska, J. X. 2016, ApJ, 829, 3
Arrigoni Battaia, F., Hennawi, J. F., Prochaska, J. X., & Cantalupo, S. 2015b, ApJ, 809, 163
Arrigoni Battaia, F., Yang, Y., Hennawi, J. F., et al. 2015a, ApJ, 804, 26
Astropy Collaboration, Robitaille, T. P., Tollerud, E. J., et al. 2013, A&A, 558, A33
Bacon, R., Accardo, M., Adjali, L., et al. 2010, Proc. SPIE, 7735, 773508
Bacon, R., Brinchmann, J., Richard, J., et al. 2015, A&A, 575, A75
Bañados, E., Decarli, R., Walter, F., et al. 2015b, ApJL, 805, L8
Bañados, E., Venemans, B., Walter, F., et al. 2013, ApJ, 773, 178
Bañados, E., Venemans, B. P., Decarli, R., et al. 2016, ApJS, 227, 11
Bañados, E., Venemans, B. P., Morganson, E., et al. 2014, AJ, 148, 14
Bañados, E., Venemans, B. P., Morganson, E., et al. 2015a, ApJ, 804, 118
Barnett, R., Warren, S. J., Banerji, M., et al. 2015, A&A, 575, A31
Barrio, F. E., Jarvis, M. J., Rawlings, S., et al. 2008, MNRAS, 389, 792
Beelen, A., Cox, P., Benford, D. J., et al. 2006, ApJ, 642, 694
Bergeron, J., Petitjean, P., Cristiani, S., et al. 1999, A&A, 343, L40
Bertin, E., & Arnouts, S. 1996, A&As, 117, 393
Bonning, E. W., Shields, G. A., & Salviander, S. 2007, ApJL, 666, L13
Borisova, E., Cantalupo, S., Lilly, S. J., et al. 2016a, ApJ, 831, 39
Borisova, E., Lilly, S. J., Cantalupo, S., et al. 2016b, ApJ, 830, 120
Bowen, D. V., Hennawi, J. F., Ménard, B., et al. 2006, ApJL, 645, L105
Bremer, M. N., Fabian, A. C., Sargent, W. L. W., et al. 1992, MNRAS, 258, 23P
Bunker, A., Smith, J., Spinrad, H., Stern, D., & Warren, S. 2003, Ap&SS, 284, 357
Cantalupo, S., Arrigoni-Battaia, F., Prochaska, J. X., Hennawi, J. F., & Madau, P. 2014, Natur, 506, 63
Cantalupo, S., Lilly, S. J., & Haehnelt, M. G. 2012, MNRAS, 425, 1992
Cantalupo, S., Porciani, C., Lilly, S. J., & Miniati, F. 2005, ApJ, 628, 61
Carnall, A. C., Shanks, T., Chehade, B., et al. 2015, MNRAS, 451, L16
Casey, C. M., Scoville, N. Z., Sanders, D. B., et al. 2014, ApJ, 796, 95
Christensen, L., Jahnke, K., Wisotzki, L., & Sánchez, S. F. 2006, A&A, 459, 717
Courbin, F., North, P., Eigenbrod, A., & Chelouche, D. 2008, A&A, 488, 91
da Cunha, E., Groves, B., Walter, F., et al. 2013, ApJ, 766, 13
De Breuck, C., Bertoldi, F., Carilli, C., et al. 2004, A&A, 424, 1
De Rosa, G., Venemans, B. P., Decarli, R., et al. 2014, ApJ, 790, 145
Decarli, R., Treves, A., & Falomo, R. 2009, MNRAS, 396, L31
Decarli, R., Walter, F., Aravena, M., et al. 2016, ApJ, 833, 70
Decarli, R., Walter, F., Venemans, B. P., et al. 2017, Natur, 545, 457
Decarli, R., Walter, F., Yang, Y., et al. 2012, ApJ, 756, 150
Di Matteo, T., Khandai, N., DeGraf, C., et al. 2012, ApJL, 745, L29
Djorgovski, S. 1991, in ASP Conf. Ser. 21, The Space Distribution of Quasars, ed. D. Crampton (San Francisco, CA: ASP), 349
Djorgovski, S. G., Courbin, F., Meylan, G., et al. 2007, ApJL, 662, L1
Dubois, Y., Pichon, C., Haehnelt, M., et al. 2012, MNRAS, 423, 3616
Edge, A., Sutherland, W., Kuijken, K., et al. 2013, Msngr, 154, 32
Eftekharzadeh, S., Myers, A. D., Hennawi, J. F., et al. 2017, MNRAS, 468, 77
Eftekharzadeh, S., Myers, A. D., White, M., et al. 2015, MNRAS, 453, 2779
Fan, X., Strauss, M. A., Richards, G. T., et al. 2006, AJ, 131, 1203
Farina, E. P., Falomo, R., Decarli, R., Treves, A., & Kotilainen, J. K. 2013, MNRAS, 429, 1267
Farina, E. P., Falomo, R., Scarpa, R., et al. 2014, MNRAS, 441, 886
Farina, E. P., Falomo, R., & Treves, A. 2011, MNRAS, 415, 3163
Farina, E. P., Montuori, C., Decarli, R., & Fumagalli, M. 2013, MNRAS, 431, 1019
Fathivavsari, H., Petitjean, P., Noterdaeme, P., et al. 2016, MNRAS, 461, 1816
Feng, Y., Di Matteo, T., Croft, R., & Khandai, N. 2014, MNRAS, 440, 1865
Fumagalli, M., Cantalupo, S., Dekel, A., et al. 2016, MNRAS, 462, 1978
Fynbo, J. U., Thomsen, B., & Møller, P. 2000, A&A, 353, 457
Gallerani, S., Maiolino, R., Juarez, Y., et al. 2010, A&A, 523, A85
Garcia-Vergara, C., Hennawi, J. F., Barrientos, L. F., & Rix, H.-W. 2017, arXiv:1701.01114
Gehrels, N. 1986, ApJ, 303, 336
Gordon, K. D., Clayton, G. C., Misselt, K. A., Landolt, A. U., & Wolff, M. J. 2003, ApJ, 594, 279
Goto, T., Utsumi, Y., Furusawa, H., Miyazaki, S., & Komiyama, Y. 2009, MNRAS, 400, 843
Goto, T., Utsumi, Y., Kikuta, S., et al. 2017, MNRAS, 470, L117
Goto, T., Utsumi, Y., Walsh, J. R., et al. 2012, MNRAS, 421, L77
Gould, A., & Weinberg, D. H. 1996, ApJ, 468, 462
Haiman, Z., & Rees, M. J. 2001, ApJ, 556, 87
Hashimoto, T., Ouchi, M., Shimasaku, K., et al. 2013, ApJ, 765, 70
Heckman, T. M., Lehnert, M. D., Miley, G. K., & van Breugel, W. 1991b, ApJ, 381, 373
Heckman, T. M., Miley, G. K., Lehnert, M. D., & van Breugel, W. 1991a, ApJ, 370, 78
Hennawi, J. F., Myers, A. D., Shen, Y., et al. 2010, ApJ, 719, 1672
Hennawi, J. F., & Prochaska, J. X. 2007, ApJ, 655, 735
Hennawi, J. F., & Prochaska, J. X. 2013, ApJ, 766, 58
Hennawi, J. F., Prochaska, J. X., Burles, S., et al. 2006a, ApJ, 651, 61
Hennawi, J. F., Prochaska, J. X., Cantalupo, S., & Arrigoni-Battaia, F. 2015, Sci, 348, 779
Hennawi, J. F., Strauss, M. A., Oguri, M., et al. 2006b, AJ, 131, 1
Herenz, E. C., Wisotzki, L., Roth, M., & Anders, F. 2015, A&A, 576, A115
Hewett, P. C., & Wild, V. 2010, MNRAS, 405, 2302
Hodge, J. A., Riechers, D., Decarli, R., et al. 2015, ApJL, 798, L18
Hu, E. M., Cowie, L. L., Barger, A. J., et al. 2010, ApJ, 725, 394
Humphrey, A., Binette, L., Villar-Martín, M., Aretxaga, I., & Papaderos, P. 2013, MNRAS, 428, 563
Hunter, J. D. 2007, CSE, 9, 90
Husband, K., Bremer, M. N., Stanway, E. R., & Lehnert, M. D. 2015, MNRAS, 452, 2388
Jiang, L., Fan, X., Bian, F., et al. 2009, AJ, 138, 305
Jiang, L., McGreer, I. D., Fan, X., et al. 2016, ApJ, 833, 222
Johnson, S. D., Chen, H.-W., & Mulchaey, J. S. 2015, MNRAS, 452, 2553
Karhunen, K., Kotilainen, J. K., Falomo, R., & Bettoni, D. 2014, MNRAS, 441, 1802
Kayo, I., & Oguri, M. 2012, MNRAS, 424, 1363
Kennicutt, R. C., & Evans, N. J. 2012, ARA&A, 50, 531
Lau, M. W., Prochaska, J. X., & Hennawi, J. F. 2016, ApJS, 226, 25
Lau, M. W., Prochaska, J. X., & Hennawi, J. F. 2017, arXiv:1705.03476
Lehnert, M. D., & Becker, R. H. 1998, A&A, 332, 514
Leipski, C., Meisenheimer, K., Walter, F., et al. 2014, ApJ, 785, 154
Lusso, E., Hennawi, J. F., Comastri, A., et al. 2013, ApJ, 777, 86
Lusso, E., Worseck, G., Hennawi, J. F., et al. 2015, MNRAS, 449, 4204
Madau, P., Haardt, F., & Dotti, M. 2014, ApJL, 784, L38
Martin, D. C., Chang, D., Matuszewski, M., et al. 2014, ApJ, 786, 106
Matsuda, Y., Yamada, T., Hayashino, T., et al. 2011, MNRAS, 410, L13
Matsuoka, Y., Onoue, M., Kashikawa, N., et al. 2016, ApJ, 828, 26
Matsuoka, Y., Onoue, M., Kashikawa, N., et al. 2017, arXiv:1704.05854
Matthee, J., Sobral, D., Santos, S., et al. 2015, MNRAS, 451, 400
Mazzucchelli, C., Bañados, E., Decarli, R., et al. 2017b, ApJ, 834, 83
Mazzucchelli, C., Bañados, E., Venemans, B. P., et al. 2017a, ApJ, in press (arXiv:1710.01251)
McGreer, I. D., Eftekharzadeh, S., Myers, A. D., & Fan, X. 2016, AJ, 151, 61
McGreer, I. D., Fan, X., Strauss, M. A., et al. 2014, AJ, 148, 73
Mechtley, M., Windhorst, R. A., Ryan, R. E., et al. 2012, ApJL, 756, L38
Meiksin, A. 2006, MNRAS, 365, 807
Merloni, A., Bongiorno, A., Brusa, M., et al. 2014, MNRAS, 437, 3550
Mortlock, D. J., Warren, S. J., Venemans, B. P., et al. 2011, Natur, 474, 616
Myers, A. D., Brunner, R. J., Nichol, R. C., et al. 2007, ApJ, 658, 85
Myers, A. D., Brunner, R. J., Richards, G. T., et al. 2007, ApJ, 658, 99
Myers, A. D., Richards, G. T., Brunner, R. J., et al. 2008, ApJ, 678, 635
North, P. L., Courbin, F., Eigenbrod, A., & Chelouche, D. 2012, A&A, 542, A91
Ouchi, M., Shimasaku, K., Furusawa, H., et al. 2010, ApJ, 723, 869
Padmanabhan, N., White, M., Norberg, P., & Porciani, C. 2009, MNRAS, 397, 1862
Peebles, P. J. E. 1980, The large-scale structure of the universe, Research supported by the National Science Foundation (Princeton, NJ: Princeton Univ. Press), 435
Pentericci, L., Carniani, S., Castellano, M., et al. 2016, ApJL, 829, L11
Prochaska, J. X., & Hennawi, J. F. 2009, ApJ, 690, 1558
Prochaska, J. X., Hennawi, J. F., Lee, K.-G., et al. 2013a, ApJ, 776, 136
Prochaska, J. X., Hennawi, J. F., & Simcoe, R. A. 2013b, ApJL, 762, L19
Prochaska, J. X., Lau, M. W., & Hennawi, J. F. 2014, ApJ, 796, 140

Rauch, M., Becker, G. D., Haehnelt, M. G., Carswell, R. F., & Gauthier, J.-R. 2013, MNRAS, 431, L68
Reed, S. L., McMahon, R. G., Banerji, M., et al. 2015, MNRAS, 454, 3952
Rees, M. J. 1988, MNRAS, 231, 91
Richards, G. T., Vanden Berk, D. E., Reichard, T. A., et al. 2002, AJ, 124, 1
Richardson, J., Zheng, Z., Chatterjee, S., Nagai, D., & Shen, Y. 2012, ApJ, 755, 30
Roche, N., Humphrey, A., & Binette, L. 2014, MNRAS, 443, 3795
Roettgering, H. J. A., van Ojik, R., Miley, G. K., et al. 1997, A&A, 326, 505
Ross, N. P., Shen, Y., Strauss, M. A., et al. 2009, ApJ, 697, 1634
Sandrinelli, A., Falomo, R., Treves, A., Farina, E. P., & Uslenghi, M. 2014, MNRAS, 444, 1835
Schaerer, D. 2002, A&A, 382, 28
Schneider, P. 2006, Extragalactic Astronomy and Cosmology (Berlin: Springer)
Selsing, J., Fynbo, J. P. U., Christensen, L., & Krogager, J.-K. 2016, A&A, 585, A87
Shen, Y., Hennawi, J. F., Shankar, F., et al. 2010, ApJ, 719, 1693
Shen, Y., McBride, C. K., White, M., et al. 2013, ApJ, 778, 98
Shen, Y., Strauss, M. A., Oguri, M., et al. 2007, AJ, 133, 2222
Smith, D. J. B., Jarvis, M. J., Simpson, C., & Martínez-Sansigre, A. 2009, MNRAS, 393, 309
Stark, D. P., Richard, J., Charlot, S., et al. 2015, MNRAS, 450, 1846
Steidel, C. C., Erb, D. K., Shapley, A. E., et al. 2010, ApJ, 717, 289
Swinbank, A. M., Vernet, J. D. R., Smail, I., et al. 2015, MNRAS, 449, 1298
Tody, D. 1986, Proc. SPIE, 627, 733
Tody, D. 1993, in ASP Conf. Ser. 52, Astronomical Data Analysis Software and Systems II, ed. R. J. Hanisch, R. J. V. Brissenden, & J. Barnes (San Francisco, CA: ASP), 173
Trainor, R., & Steidel, C. C. 2013, ApJL, 775, L3
Treister, E., Krolik, J. H., & Dullemond, C. 2008, ApJ, 679, 140
Valiante, R., Schneider, R., Salvadori, S., & Bianchi, S. 2011, MNRAS, 416, 1916
van Ojik, R., Roettgering, H. J. A., Miley, G. K., & Hunstead, R. W. 1997, A&A, 317, 358
Venemans, B. P., Bañados, E., Decarli, R., et al. 2015b, ApJL, 801, L11
Venemans, B. P., Findlay, J. R., Sutherland, W. J., et al. 2013, ApJ, 779, 24
Venemans, B. P., McMahon, R. G., Walter, F., et al. 2012, ApJL, 751, L25
Venemans, B. P., Röttgering, H. J. A., Miley, G. K., et al. 2007, A&A, 461, 823
Venemans, B. P., Verdoes Kleijn, G. A., Mwebaze, J., et al. 2015a, MNRAS, 453, 2259
Venemans, B. P., Walter, F., Zschaechner, L., et al. 2016, ApJ, 816, 37
Volonteri, M. 2010, A&Ar, 18, 279
Volonteri, M. 2012, Sci, 337, 544
Volonteri, M., & Rees, M. J. 2005, ApJ, 633, 624
Volonteri, M., Silk, J., & Dubus, G. 2015a, ApJ, 804, 148
Weidinger, M., Møller, P., & Fynbo, J. P. U. 2004, Natur, 430, 999
Weidinger, M., Møller, P., Fynbo, J. P. U., & Thomsen, B. 2005, A&A, 436, 825
Weilbacher, P. M., Streicher, O., Urrutia, T., et al. 2012, Proc. SPIE, 8451, 84510B
Weilbacher, P. M., Streicher, O., Urrutia, T., et al. 2014, in ASP Conf. Ser. 485, Astronomical Data Analysis Software and Systems XXIII, ed. N. Manset & P. Forshay (San Francisco, CA: ASP), 451
White, M., Myers, A. D., Ross, N. P., et al. 2012, MNRAS, 424, 933
Willott, C. J., Chet, S., Bergeron, J., & Hutchings, J. B. 2011, AJ, 142, 186
Willott, C. J., Delorme, P., Reylé, C., et al. 2010, AJ, 139, 906
Wisotzki, L., Bacon, R., Blaizot, J., et al. 2016, A&A, 587, A98
Yang, Y., Zabludoff, A., Tremonti, C., Eisenstein, D., & Davé, R. 2009, ApJ, 693, 1579
Yoo, J., & Miralda-Escudé, J. 2004, ApJL, 614, L25
Zhang, S., Wang, T., Wang, H., & Zhou, H. 2013, ApJ, 773, 175
Zirm, A. W., Overzier, R. A., Miley, G. K., et al. 2005, ApJ, 630, 68